

# Paleomagnetic investigation of the basal Maieberg Formation (Namibia) cap carbonate sequence (635 Ma): Implications for Snowball Earth postglacial dynamics

#### Thales Pescarini<sup>1,†</sup>, Ricardo I.F. Trindade<sup>1</sup>, Paul F. Hoffman<sup>2,3</sup>, and Lucy Gomes Sant'Anna<sup>4</sup>

<sup>1</sup>Department of Geophysics, University of São Paulo, São Paulo, São Paulo 05508-080 Brazil

#### ABSTRACT

In this study, we investigate the paleomagnetism of the basal Maieberg Formation (Namibia) cap carbonate sequence to elucidate its magnetic properties and paleolatitude of deposition, establish global correlations, and contribute to the understanding of Snowball Earth postglacial dynamics. Two distinct magnetization components,  $C_1$  and  $C_2$ , were identified.  $C_1$  is interpreted as a depositional or post-depositional remanent magnetization carried by detrital pseudo-single domain (PSD) magnetite, while the  $C_2$  component is a thermochemical remanent magnetization carried by fine authigenic single domain (SD)-PSD magnetite. The deposition paleolatitude provided by  $C_1$  is 33.3°  $\pm$  3.2°, which gives an initial quantitative approximation of the paleolatitude for the underlying Marinoan Ghaub diamictites. The thickness of the Keilberg Member cap dolostone is anomalously high for the paleolatitude calculated with  $C_1$ , which suggests that other factors besides the influence of the paleolatitude on carbonate oversaturation may have influenced the sedimentary production of cap dolostones and the overall thickness of the flooding cap carbonate sequence. Possible explanations could include the influence of alkalinity input combined with local tectonic subsidence during a long glacial period with unusually low sedimentation rates, which appear to be in a favorable configuration for the substantial thickness of the Keilberg Member. Paleomagnetic field reversals at the Keilberg cap dolostone and analogous units

Thales Pescarini https://orcid.org/0000-0001 -6130-6546 †thales.pescarini@usp.br

globally suggest a longer duration of marine transgression than energy-balance deglaciation models and sedimentological-geochemical observations have constrained. Factors such as ocean warming, thermal expansion, and local glacio-isostatic adjustments imply extended marine transgressions beyond the deglaciation period. Still, magnetostratigraphic estimates for postglacial transgressive sequences require longer time scales by a factor of five or more. Thus, the conflict arising between estimates derived from paleomagnetic data and the constraints imposed by climate physics underscores uncertainties regarding an unconventional field state or a remanence acquisition mechanism within these cap carbonates that is not fully understood. Importantly, if such a phenomenon proves to be primary and global, the widespread occurrence of these stratigraphically compressed reversals would support the precise temporal correlation between Marinoan cap dolostones. The  $C_2$  pole correlates with Cambrian remagnetization poles observed in carbonates from West Gondwana, which now extend to the Congo craton. The remanence acquisition of  $C_2$  likely stems from diagenesis-related low-temperature authigenic magnetite formation after the conversion of iron-rich smectite to iron-poor illite. Cooling associated with the Kaoko orogen's exhumation and tectonic uplift possibly locked the magnetic system at ca. 520 Ma, supported by the  $C_2$  pole position on the West Gondwana apparent polar wander path, although other explanations remain valid.

#### 1. INTRODUCTION

During the Cryogenian period (ca. 720–635 Ma), two instances occurred in which glacial

deposits were overlain by the sudden and massive precipitation of thick carbonate sequences referred to as cap carbonates. Carbonate formations typically develop in low-latitude regions of the planet under warm aquatic conditions (Opdyke and Wilkinson, 1990; Millero, 1979; Jiang et al., 2015). Hence, the presence of both glacial and carbonate rocks indicates a climatic state markedly distinct from any observed during the Phanerozoic eon (Hoffman et al., 1998).

Corroborated by an extensive assemblage of sedimentological, geochemical, paleomagnetic, and geochronological evidence, this phenomenon converges with the Snowball Earth (SBE) hypothesis (Kirschvink, 1992; Hoffman and Schrag, 2002). This hypothesis advances the notion that over the Cryogenian epoch, Earth's oceans and a substantial portion of its continental landmasses underwent two glaciation episodes: the Sturtian glaciation (ca. 717–659 Ma) and the Marinoan glaciation (ca. 645–635 Ma). These glaciations extended the ice sheets from polar latitudes to the equatorial belt.

The extended periods of extensive ice coverage significantly reduced silicate weathering, while seafloor weathering was limited by the cold seawater temperature, although it gradually increased due to ongoing ocean acidification during the Snowball Earth episodes. This led to a substantial buildup of atmospheric CO<sub>2</sub> over millions of years spanning the cryochrons (Le Hir et al., 2008). Additionally, this environmental shift triggered increased runoff and the presence of meteoric waters with lower pH levels. Notably, the decrease in pH was not solely due to runoff; CO2 was also directly released into seawater through mid-oceanic-ridge volcanism, which was a significant factor during Snowball Earth conditions. This period also coincided with a lowered sea level (Higgins and Schrag, 2003; Le Hir et al., 2009).

GSA Bulletin; November/December 2024; v. 136; no. 11/12; p. 4775–4797; https://doi.org/10.1130/B37378.1. Published online 23 April 2024

<sup>&</sup>lt;sup>2</sup>Department of Earth and Planetary Sciences, Harvard University, Cambridge, Massachusetts 02138, USA

<sup>&</sup>lt;sup>3</sup>School of Earth and Ocean Sciences, University of Victoria, Victoria, British Columbia V8P 3E6, Canada

<sup>&</sup>lt;sup>4</sup>Brazilian Institute of Energy and Environment, University of São Paulo, São Paulo, São Paulo 05508-900, Brazil

Ultimately, these interconnected factors converged to facilitate extensive weathering of pre-Snowball Earth highly reactive carbonate platforms. Substantial quantities of highly reactive rock powder, including carbonate rock powder exposed through glacial abrasion and deglaciation, played a pivotal role. The heightened reactivity of glacial rock powder stemmed from its exceptionally high surface-to-volume ratio. As a consequence of these processes, a significant amount of alkalinity was introduced into the meltwater lid during the deglaciation phase. This complex interplay ultimately led to an extensive oversaturation of CaCO3 in the ocean, with levels sufficient to precipitate significant carbonate deposits over the glaciogenic rocks, which generated the cap carbonates (Hoffman, 2011).

Paleomagnetic records showing magnetization vectors with low inclinations, indicative of low paleolatitudes, have been documented within a considerable number of glacial deposits from both the Sturtian and Marinoan glaciations across various cratons (e.g., Evans, 2000; Trindade and Macouin, 2007; Hoffman and Li, 2009; Evans and Raub, 2011). However, despite the abundance of such records, highly reliable poles derived directly from glacial units remain very limited in number. Evans and Raub's comprehensive review in 2011 highlighted that merely two glacial units present robust data displaying this characteristic. These units are the Marinoan Elatina Formation in Southern Australia (Schmidt and Williams, 1995; Sohl et al., 1999) and the Marinoan Nantuo Formation in South China (Zhang and Piper, 1997; Zhang et al., 2013). Nonetheless, a substantial body of "moderately reliable" paleomagnetic evidence directly sourced from glacial deposits, combined with high-quality data inferred from volcanic units temporally associated with glacial periods (e.g., Franklin Large Igneous Province data from Denyszyn et al., 2009), robustly supports the occurrence of SBE events and the low paleolatitude positioning of many Cryogenian glacial deposits (Evans and Raub, 2011).

It should be noted, however, that precise paleogeographic determinations are most accurately constrained when paleomagnetic data are acquired directly from, or are in close geographic proximity to, the targeted geological units. Consequently, data sourced directly from glacial deposits or their linked cap carbonates remain of great significance. As an example, the Congo–São Francisco craton lacks any definitive reference poles that could precisely constrain its paleolatitude during the Cryogenian (Trindade et al., 2021).

On the other hand, the paleomagnetic data obtained from cap carbonates present certain challenges due to the limited number of stud-

ies, particularly when considering factors like regional extension (i.e., multiple sampled sections) and stratigraphic control. Noteworthy results indicating relatively low paleolatitudes (<40°) have been obtained in different locations, including Brazil (Mirassol d'Oeste cap dolostone; Trindade et al., 2003), Oman (Hadash cap dolostone; Kilner et al., 2005), Southern Australia (Nuccaleena cap carbonate; Schmidt et al., 2009), and South China (Doushantuo cap carbonate; Zhang et al., 2015). However, the reliability of these paleomagnetic data is problematic, as only the Nuccaleena Formation has undergone a convincing fold test, while the remaining units lack such tests or exhibit folding events that are considerably more recent than the cap formation itself.

Importantly, all of these cap carbonates exhibit more than one geomagnetic reversal, primarily concentrated in their basal cap dolostone levels, which corresponds to the transgressive system tract (TST) sequence. This phenomenon has sparked interest due to the potential for establishing correlations and investigating synchronicity among these time polarities, and also prompts questions about the timing of deposition, assuming a knowledge of the duration required for these reversals to occur. Ice-sheet melting and Quaternary analog models (Hyde et al., 2000; Peltier et al., 2004) suggest a relatively rapid deglaciation process (Hoffman et al., 2007), occurring over  $\sim 10^4$  yr. Consequently, it is inferred that the cap dolostones were formed within this timeframe during sea-level rise.

However, the presence of the reversals has prompted some authors to propose significantly longer depositional times (>105 yr), and consequently, a much slower sedimentation rate (Li, 2000; Trindade et al., 2003; Kilner et al., 2005; Raub and Evans, 2005; Schmidt et al., 2009). This is due to estimates from core conductivity (Gubbins, 1999), which suggest that the minimal time scale for a reversal is  $\sim$ 3–5 k.y. Considering that the expression of reversals within these cap dolostones spans just a few centimeters, a relatively sluggish sedimentation rate is implied. Conversely, this slower rate contradicts not just the deglaciation models but also conflicts with various sedimentary features (such as giant wave ripples; Allen and Hoffman, 2005), which gives rise to an unresolved controversy between geophysical and geological data that has persisted for decades.

Opting for a scenario with a high sedimentation rate would result in an exceptionally elevated recorded reversal rate in these cap carbonates. Unfortunately, the precise rate of geomagnetic field reversals during the formation age of these caps is largely unknown, which makes it challenging to test this hypothesis. Nevertheless,

evidence indicates that Earth's magnetic field during the Neoproterozoic was atypical in terms of field geometry, reversal rate, and paleointensity (e.g., Abrajevitch and Van der Voo, 2010; Levashova et al., 2021; Kodama, 2021; Bono et al., 2019; Lloyd et al., 2021), which would align with such a scenario.

In this study, we examined the Maieberg Formation cap carbonates in northern Namibia (Congo craton), which overlay the Ghaub Formation diamictites-a cornerstone of the SBE hypothesis (Hoffman et al., 1998; Hoffman and Schrag, 2002; Hoffman et al., 2021)—yet lack paleomagnetic data. Our objectives included (1) quantitatively determining the paleolatitude at which these rocks were formed, (2) establishing the timing of deposition and sedimentation rate, (3) elucidating the mechanisms behind remanence acquisition, and (4) establishing connections with existing paleomagnetic data from analogous units. We anticipate that these endeavors will lead to advancements in our understanding of the dynamics behind postglacial SBE.

### 2. GEOLOGICAL CONTEXT AND SAMPLING

Ca. 800-770 Ma, the southern Congo craton underwent a rifting process (Miller, 1983) that was followed by a passive margin subsidence phase until ca. 580 Ma due to thermal relaxation of the crust (Halverson et al., 2005; Goscombe et al., 2005; Gray et al., 2006). During this phase, the deposition of 2-4 km of primarily shallowwater carbonate rocks, forming the Otavi Group, occurred at the southwestern edge of the Congo craton (Hoffman and Halverson, 2008; Hoffman, 2011; Hoffman, 2021). Subsequently, during the late Ediacaran to the Cambrian, the Otavi platform became an active margin due to tectonic convergence between the Congo and Kalahari cratons to the south, and the South American continental blocks to the west, which led to the development of the Damara and Kaoko orogens, respectively (Goscombe et al., 2005; Gray et al., 2008; Oyhantçabal et al., 2009).

Stratigraphically, the Otavi platform can be divided into two distinct phases: the initial phase, which is characterized by accommodation within a rift-dominated basin, followed by the subsequent phase during the passive margin's thermal subsidence (Fig. 1). The former is evident in the Devede and Okakuyu formations of the Ombombo Subgroup, as well as the Gruis and Rasthof formations of the Abenab Subgroup, which exhibit the active influence of faulting accompanied by erosion and the presence of "cannibalized" clastics (syn-rift). The beginning of the latter phase is marked by the Ombaatjie Formation, during which a carbonate sequence

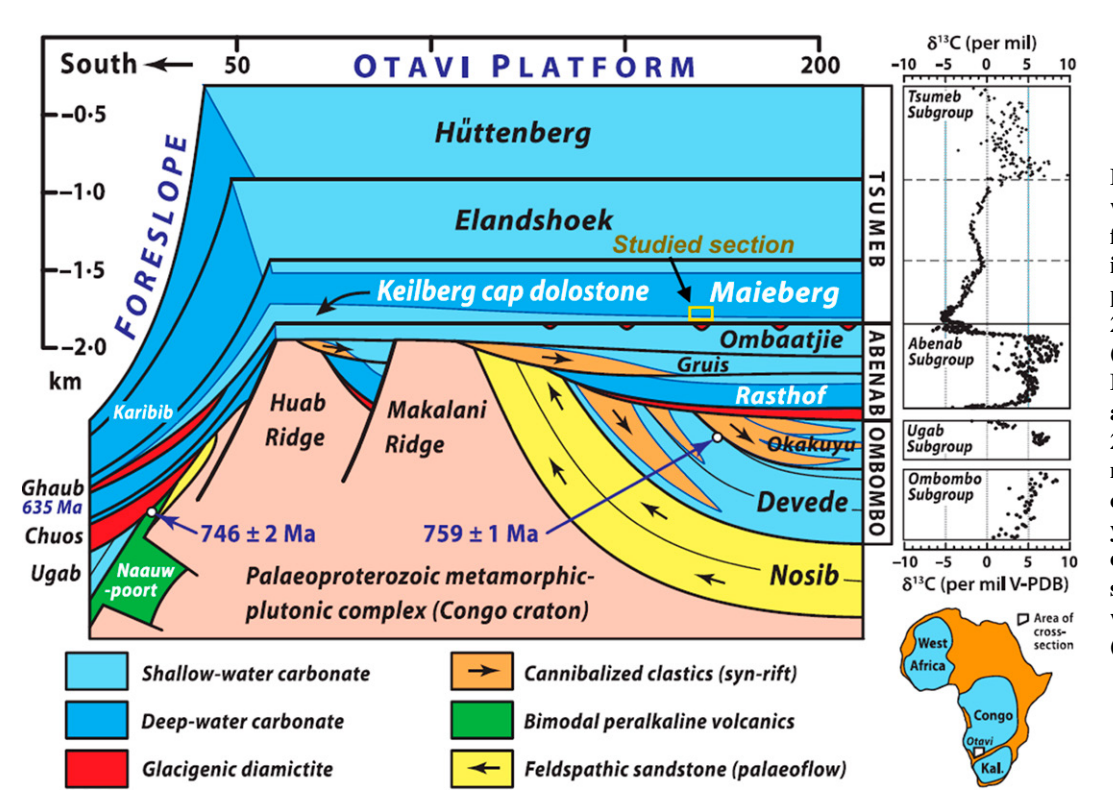


Figure 1. Stratigraphy of the western Otavi platform and foreslope with a  $\delta^{13}$ C composite profile on the right (isotopic data from Halverson et al., 2005). Age data:  $746 \pm 2$  Ma (Hoffman et al., 1996),  $759 \pm 1$ Ma (Halverson et al., 2005), and 635 Ma (Hoffmann et al., 2004). Arrows within the formations indicate the direction of sediment transport; little yellow box approximately indicates the position of the section studied in this paper. Figure was modified from Hoffman (2011).

of  $\sim$ 2 km thickness was conformably deposited (Hoffman, 2011; Hoffman et al., 2021).

Within these carbonate successions, two glaciogenic strata are observed: the Sturtian Chuos Formation (Gevers, 1931), which is dated to a maximum age of  $746 \pm 2$  Ma by Hoffman et al. (1996), and the Marinoan Ghaub Formation, which is well-constrained temporally by a U-Pb zircon age of  $635.6 \pm 0.5$  Ma (Hoffmann et al., 2004). Each glacial unit is associated with its own cap carbonate, conformably but abruptly juxtaposed, with no discernible evidence of significant temporal hiatus (Hoffman et al., 2007). Overlying the Chuos Formation are the Rasthof Formation carbonates, while overlying the Ghaub Formation is the Maieberg Formation, which is the focus of this paper.

The Maieberg cap carbonate sequence can be divided into three segments: the basal syndeglacial cap dolostone (Keilberg Member), the maximum flooding middle limestone rhythmite, and the highstand upper dolostone (Hoffman and Schrag, 2002). The Keilberg Member is a pale gray to pinkish gray dolostone that conformably rests on the Ghaub Formation or Ombaatjie Formation on the platform where the Ghaub Formation is widely absent (Fig. 1), and it averages  $\sim 38$  m in thickness. The member features pelloidal to micropelloidal textures and sedimentary structures like sheet-crack cement (slope facies only, not observed on the platform; Hoffman and Macdonald, 2010), stro-

matolites, vertical tubular structures, low-angle cross-bedding, and highly aggradational giant wave ripples, which are common to Marinoan cap dolostones. The Keilberg Member transitions conformably into the middle limestone, and initially displays a limestone-marl rhythmite at the contact that evolves upward into predominantly pure limestone rhythmite with hummocky cross-stratification near the top. The sequence culminates in the highstand dolostone, which is initially allodapic with thin layers like the underlying limestone, and evolves into more massive grainstone that becomes coarser upward, and ends with a highly silicified exposure surface. This surface is overlain by numerous tepee cycles of the lower Elandshoek Formation (Hoffman, 2011).

Sampling was conducted along the Hoanib River escarpments in northern Namibia, within the inner platform zone of the Otavi Group (Figs. 1 and 2). This zone was chosen for paleomagnetic sampling due to its expected higher detrital input, which enhances the probability of obtaining a primary direction. Our focus was on the Keilberg dolostones and immediately overlying limestone, where we aimed to capture a paleomagnetic direction closely related to glaciogenic rocks and detect potential reversals near the contact, analogous to other cap carbonates. Two sections (A and B) from a synform with a NE–SW axial plane were collected for a fold test (Fig. 2). The orientation and position of the

fold suggest that it resulted from the main Kaokoan folding phase, which occurred between 580 Ma and 570 Ma (Goscombe et al., 2005; Goscombe et al., 2018). In section A (sites 1–9), we collected samples at 20 cm intervals, comprehensively covering Keilberg Member facies variations. Section B (site 10) involved sampling every 2 m, up to 20 m in height. The lithology comprised micropeloidal gray or pinkish gray dolostones transitioning to laminated gray limestones at the top. Notably, we observed stromatolites with tubular structures of between 2 m and 7 m, followed by pseudo-tepees from 8 m to 12 m in length. A gasoline-powered portable drill with a nonmagnetic diamond drill bit was used for sampling, aided by solar and magnetic Pomeroy compasses for field orientation. Ultimately, we collected 93 samples from section A and 13 from section B (designated as collection NA sites, Table 1), which were subsequently transformed into 128 standard-format paleomagnetic specimens (2.2 cm in height).

#### 3. METHODS

## **3.1.** Paleomagnetism and Magnetic Mineralogy

Paleomagnetic and rock magnetic measurements were conducted at the Paleomagnetism and Rock Magnetism Laboratory (USPMag) within the Institute of Astronomy, Geophys-

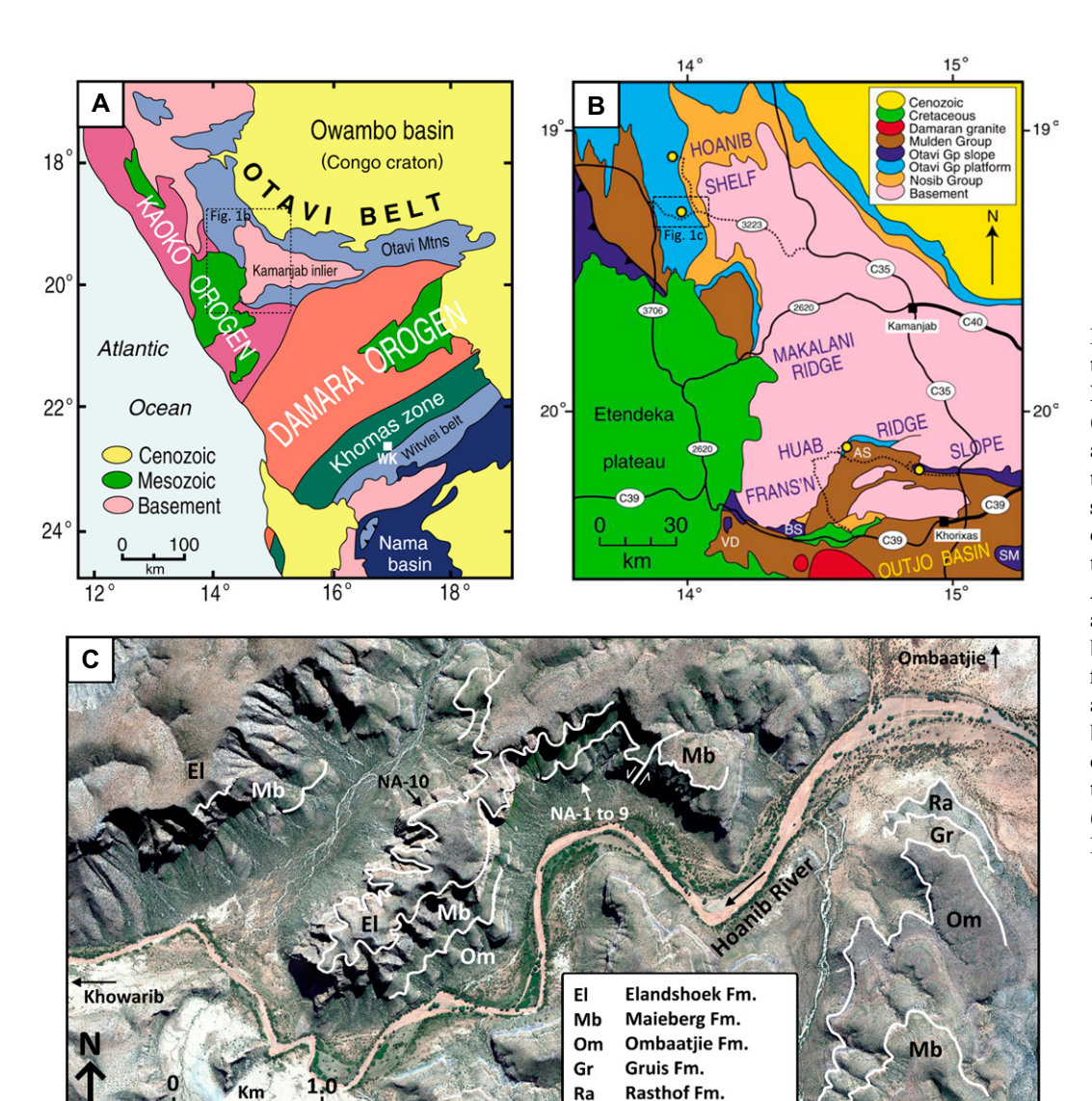


Figure 2. (A) Tectonic zonation of central and northern Namibia. WK-Windhoek. (B) Geology and access roads around the western syntaxis of the Otavi fold belt. AS-Achas syncline; BS-Bethanis syncline; SM-Summas Mountains; VD—Vrede domes. (C) Aerial photo of the sampling area on Hoanib shelf at Ombaatjie. Contacts between the formations are drawn in white, and the sampling sections on both sides of the cliff are indicated by arrows. NA-1-9 (section A) and NA-10 (section B). (Extracted and redrawn from Hoffman, 2002).

ics, and Atmospheric Sciences at the University of São Paulo (USP) in São Paulo, Brazil. The remanence measurements were performed using a 2G Enterprises cryogenic magnetometer equipped with a direct current sensor and automatic horizontal device. Thermal stepwise

demagnetizations were performed utilizing a Magnetic Measurements, Inc., paleomagnetic oven, employing 50 °C increments from room temperature to 300 °C, and 20 °C increments up to 600 °C or until complete demagnetization occurred. Hysteresis loops, isothermal

Table 1. Sampling data										
Site	φ <b>(s)</b>	\(s)	n	С	Elevation (m)	Section				
NA-1	14.0°E	19.3°S	8	C <sub>1</sub>	0-1.75	A				
NA-2 NA-3			15 7	C₁ C₁	1.75–4.50 4.50–5.70	A				
NA-4			10	$C_1$	5.70–6.81	Â				
NA-5			4	Č,	6.81-7.30	A				
NA-6			20	C <sub>1</sub>	7.30-12.56	Α				
NA-7			21	$C_2$	12.56-18.69	Α				
NA-8			8	$C_2$	18.69-27.95	Α				
NA-9			No results	No results	2.00-18.50	Α				
NA-10			13	$C_1 + C_2$		В				

*Note:*  $\varphi(s)$  and  $\lambda(s)$  are the longitude and latitude of the site; n is the number of samples; C is the magnetization component verified at the site. The elevation has zero value relative to the base of the sampled section.

remanent magnetization (IRM) curves, and first-order reversals curves (FORCs) were acquired using a Princeton Measurements Corporation MicroMag 3900 Series vibrating sample magnetometer. Magnetization component identification was achieved through vector analysis (Zijderveld, 1967) and principal component analysis (PCA) (Kirschvink, 1980). Calculation of mean directions and statistical parameters employed Fisher's (1953) statistics. Component separation criteria involved a minimum of demagnetization steps computed at the mean  $(n) \ge 4$  and a maximum angular deviation (MAD) of  $\leq 13^{\circ}$ . The paleomagnetic poles were calculated on a sample basis. Although subsections were sampled in different portions (laterally), and labeled as sites for sample control, they belong to the same section, and we do not consider it meaningful to consider them as sites for the purpose of mean calculation (see the Supplemental Material<sup>1</sup>). The PmagPy software package (Tauxe et al., 2016) was employed for PCA analysis, hysteresis data processing, bootstrap fold, and reversal tests. Bayesian reversal tests followed the approach of Heslop and Roberts (2018). FORCs data were processed using the FORCsensei package developed by Heslop et al. (2020). IRM processing and component unmixing utilized the MAX UnMix program (Maxbauer et al., 2016). The GPlates package was used for paleomagnetic pole analysis (Boyden et al., 2011). The paleomagnetic remanence measurements involved 105 specimens, while hysteresis loops, FORCs, IRM acquisition, and IRM unmix processing were carried out in 17, 8, 17, and 9 samples, respectively.

#### 3.2. X-Ray Diffraction (XRD)

XRD was conducted at the Petroleum Systems Rock Characterization Laboratory within the Institute of Energy and Environment (IEE/USP). The analysis utilized a Bruker D8 ADVANCE diffractometer equipped with a LYNXEYE XE detector and theta-theta system. Cu K alpha radiation was employed, with parameters set at 40 kV, 25 mA, and automatic air-scatter. Primary slits were adjusted to 0.5 mm, secondary slits to 1.0 mm, the collimator at 2.5°, and an Ni filter was applied. The scan spanned from 2°  $2\theta$  to  $100^{\circ}$   $2\theta$ , with increments of  $0.02^{\circ}$  and an acquisition time of 3.1 s per step. Mineral identification and graphical interpretation of diffractograms were accomplished using DiffracEva software version 4.2.2 (Bruker ASX GmbH), complemented by identification sheets from the International Center for Diffraction Data (ICDD). Prior to analysis, samples were ground to fine sand grain size using an agate mill. A total of 16 samples, encompassing both dolostone and limestone, underwent XRD assessment.

#### 3.3. Scanning Electron Microscopy (SEM)

SEM observations were conducted at two laboratories within the University of São Paulo. Initial observations were made at the Technological Characterization Laboratory (LCT/USP), with a Quanta 650 FEG electron microscope integrated with a Quantax (Bruker) energy-dispersive spectroscopy (EDS) system. These observations were carried out at a beam voltage of 15 kV with a sample distance of  $\sim\!14$  mm. Subsequent observations were made at

the Electron Microscopy Laboratory (Labmev) of the Geosciences Institute (IGc/USP), utilizing a LEO 440i electron microscope, combined with an Si(Li) solid-state detector EDS system and Oxford Instruments' Inca software. Besides EDS, secondary electron and backscattered electron detectors were engaged under beam voltage conditions of 20 kV, with sample distances ranging from 18 mm to 28 mm. To enhance sample quality, gold coating was achieved through sputtering using an Emitech sputter coater model K550, while carbon coating was accomplished through an evaporation process using a Jeol electron microscopy evaporator. The SEM and EDS analyses were performed on a set of six dolostone and limestone samples.

#### 4. RESULTS

#### 4.1. Paleomagnetism

Two distinct characteristic remanent magnetization vectors were identified in our samples and are designated here as component 1  $(C_1)$  and component 2  $(C_2)$  (Fig. 3; Tables 1 and 2). The  $C_1$  component was exclusively observed in the lower portion of the Keilberg Member dolostones, which extend to  $\sim$ 13 m above the contact with the diamictites. Conversely, the  $C_2$  component is present in both the dolostone and limestone layers situated above the 13 m mark (Fig. 4).

 $C_1$  displays a dual polarity, featuring directions of northeast (southwest) declinations along with negative (positive) inclinations (Fig. 3). The Zijderveld diagrams of this component predominantly exhibit a univectorial nature, although in certain samples, a secondary component becomes detectable upon demagnetization at temperatures of <200 °C. This low-temperature component aligns closely with the present-day geomagnetic field (PDF) and is attributed to the influence of viscous magnetization acquisition.

The demagnetization procedure effectively eliminates  $C_1$  until maximum temperatures of  $\sim$ 550 °C are reached. The computed average direction for vectors displaying positive inclinations is characterized by a declination  $(D_m)$  of  $210.1^\circ$ , inclination  $(I_m)$  of  $36.1^\circ$ , angle of 95% confidence cone  $(\alpha_{95})$  of  $10.5^\circ$ , and a precision parameter (k) of 28.65. Conversely, the mean direction for vectors with negative inclinations is represented by  $D_m = 19.6^\circ$ ,  $I_m = -42.8^\circ$ ,  $\alpha_{95} = 10.2^\circ$ , and k = 18.92. Notably, the  $C_1$  negative inclination polarity is distinct from the PDF  $(D = 339^\circ, I = -58.4^\circ)$  and dipolar field (DF)  $(D = 0^\circ, I = -35.0^\circ)$  directions at the 95% confidence level (Fig. 3).

 $C_2$  exhibits solely positive inclination vectors, which are directed toward the north-north-

west. Following the removal of the identical viscous magnetization at 200 °C, this component becomes distinct. Across most specimens, complete demagnetization of  $C_2$  occurs at temperatures below 450 °C (Fig. 3). This component yields an average orientation characterized by  $D_m = 344.7^\circ$ ,  $I_m = 53.9^\circ$ ,  $\alpha_{95} = 4.3^\circ$ , and k = 44.0.

The inherently weak natural remanent magnetization (NRM) of all samples falls within the range of  $10^{-6}$  A/m to  $5 \cdot 10^{-4}$  A/m. Notably, during the demagnetization process of  $C_1$ , the vector projections exhibit a relatively noisy pattern in contrast to the more consistent diagrams observed for  $C_2$  (Fig. 3). This behavior is attributed to the generally lower remanent magnetization intensity of  $C_1$ -bearing rocks than that of  $C_2$ -bearing rocks. Consequently, the demagnetization signal from  $C_1$ -bearing rocks tends to be noisier and less stable.

Of particular significance is the observed trend in the NRM intensity curve, which displays a generally gradual increase toward the upper levels (Fig. 4). This trend aligns roughly with the corresponding behavior of the high-field mass-normalized magnetic susceptibility ( $\chi_{hf}$ ) derived from the inclination of hysteresis loops measured at high field strengths (>700 mT). With these components determined, we subsequently subjected them to fold and reversal tests to ascertain their primary or secondary natures.

 $C_1$  exhibits dual polarity, which allows for the implementation of a reversal test. In the scenario where the component of the dual polarity is primary, we anticipate observing consistent stratigraphic reversals. In other words, polarity zones should exhibit stratigraphic cohesiveness rather than random occurrences of normal and reverse polarities at the same stratigraphic level (Butler, 1992). Such coherence in polarity is evident in the  $C_1$  sequence (Fig. 4).

Additionally, employing statistical reversal tests facilitates the identification of secondary magnetization components that could introduce bias to the antipodal characteristics of polarity groups within an axisymmetric geomagnetic field. To address this, we conducted two distinct independent reversal tests using the bootstrap (Tauxe et al., 1991) and Bayesian statistics (Heslop and Roberts, 2018). Employing the bootstrap approach, both polarities display an overlap in all three Cartesian coordinates at a 95% confidence level (Fig. 5), thereby yielding a positive test. Adhering to the methodology outlined by Heslop and Roberts (2018), the calculated Bayes factor (BF) for the hypothesis asserting a common mean for the two polarity sets is 3.10. Correspondingly, the associated hypothesis probability,  $p(H_A|X)$ , is 76%, which is indicative of a

<sup>&</sup>lt;sup>1</sup>Supplemental Material. Complementary rock magnetism information and sample-level directional statistics. Please visit https://doi.org/10.1130/GSAB .S.25571712 to access the supplemental material; contact editing@geosociety.org with any questions.

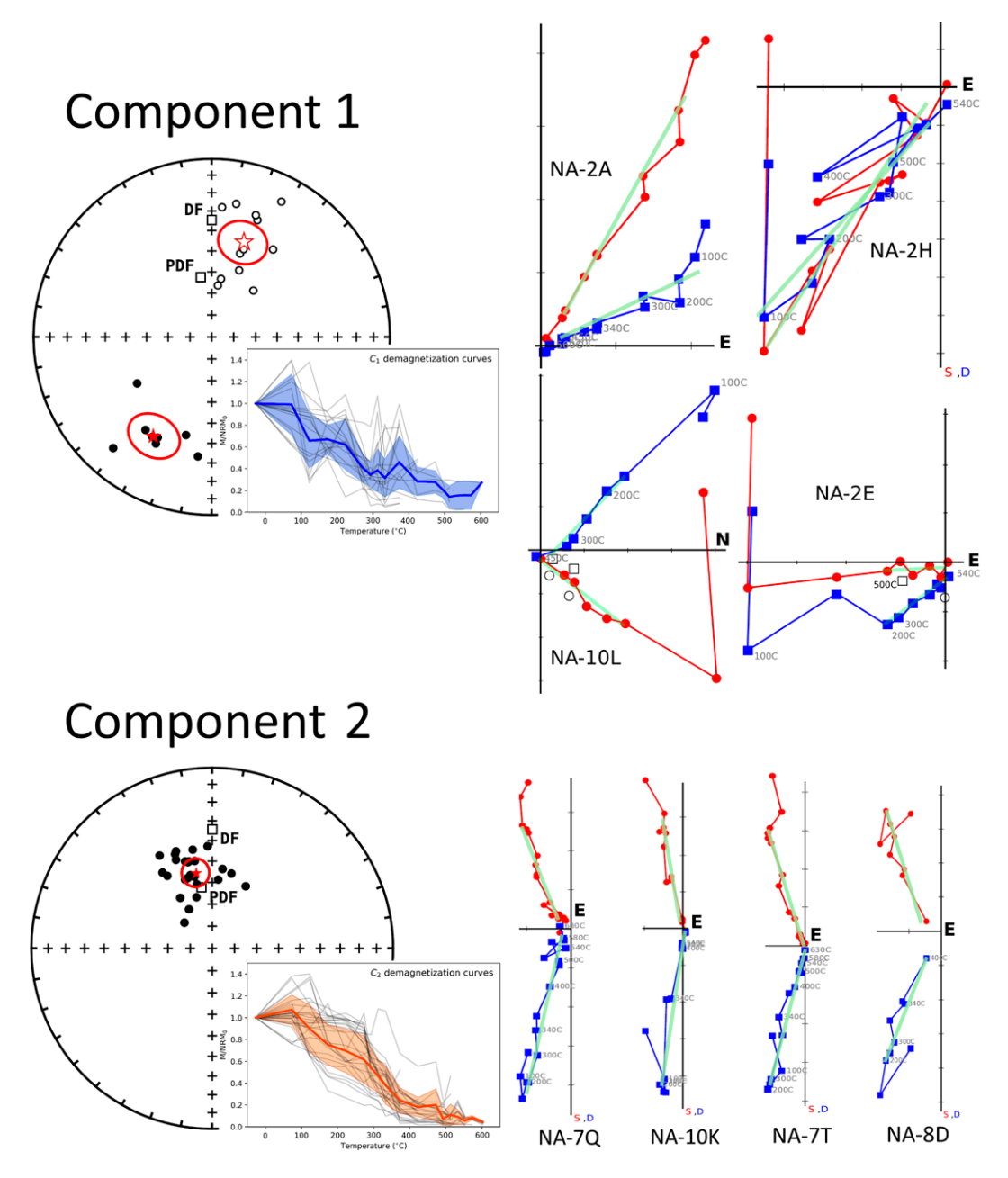


Figure 3. Mean characteristic directions of the remanent magnetization components discretized in the Maieberg carbonates (red stars) and associated  $\alpha_{95}$ s (red ellipses). Closed (open) symbols indicate downward (upward) directions in the stereographic projections. Squares are the present-day field (PDF) and dipolar field (DF) directions on sampling locations, respectively. Graphs below the stereograms are the individual demagnetization curves (thin gray), the average of the curves (thick blue/orange), and the error (blue/orange shaded area). On the right are representative Zijderveld diagrams (bluevertical projection; red-horizontal projection).

common mean with positive support as per Raftery (1995). This result contributes an additional independent positive reversal test.

We also conducted fold tests (Graham, 1949) for both components. In this context, we employed the bootstrap method introduced by

Tauxe and Watson (1994), wherein the degree of clustering in directions during the unfolding process is indicated by the magnitude of the maximum eigenvalue ( $\tau_1$ ) of the orientation matrix derived from pseudo-samples representative of the distribution of directions.

TABLE 2. PALEOMAGNETIC DATA

С	$D_m$	I <sub>m</sub>	$\alpha_{95}$	k	φ <b>(p)</b>	λ(ρ)	dp	dm
C <sub>1</sub>	24.5°	-40.8°	7.28°	21.05	298.4°E	66.8°S	8.97°	14.80°
C <sub>1</sub> (unfolded)	47.69°	-52.82°	7.26°	21.15	312.0°E	45.37°S	6.95°	10.06°
C <sub>2</sub>	344.7°	53.9°	4.3°	44.0	358°E	34.32°N	4.21°	6.01°

Note: C—magnetization component;  $D_m$ —mean declination;  $I_m$ —mean inclination;  $\alpha_{95}$ —angle of 95% confidence cone; k—precision parameter;  $\varphi(p)$  and  $\lambda(p)$ —pole longitude and latitude; dp and dm—pole confidence ellipse semi-axis.

For  $C_1$ , the highest value of  $\tau_1$  occurs within an unfolding range of -10% to 51% (Fig. 6). This result raises certain issues that necessitate clarification prior to interpretation. Initially, it should be noted that the  $C_1$  paleomagnetic directions are nearly parallel to the fold hinge line. This characteristic diminishes the test's efficacy due to the limited impact of rotation on the vectors. Consequently, the key Fisher statistical parameters k and  $\alpha_{95}$  of the mean vectors exhibit minimal alteration both pre- and post-tectonic correction (Table 2). Furthermore, due to practical field constraints and sampling procedures, a substantial majority (90%) of isolated  $C_1$ 

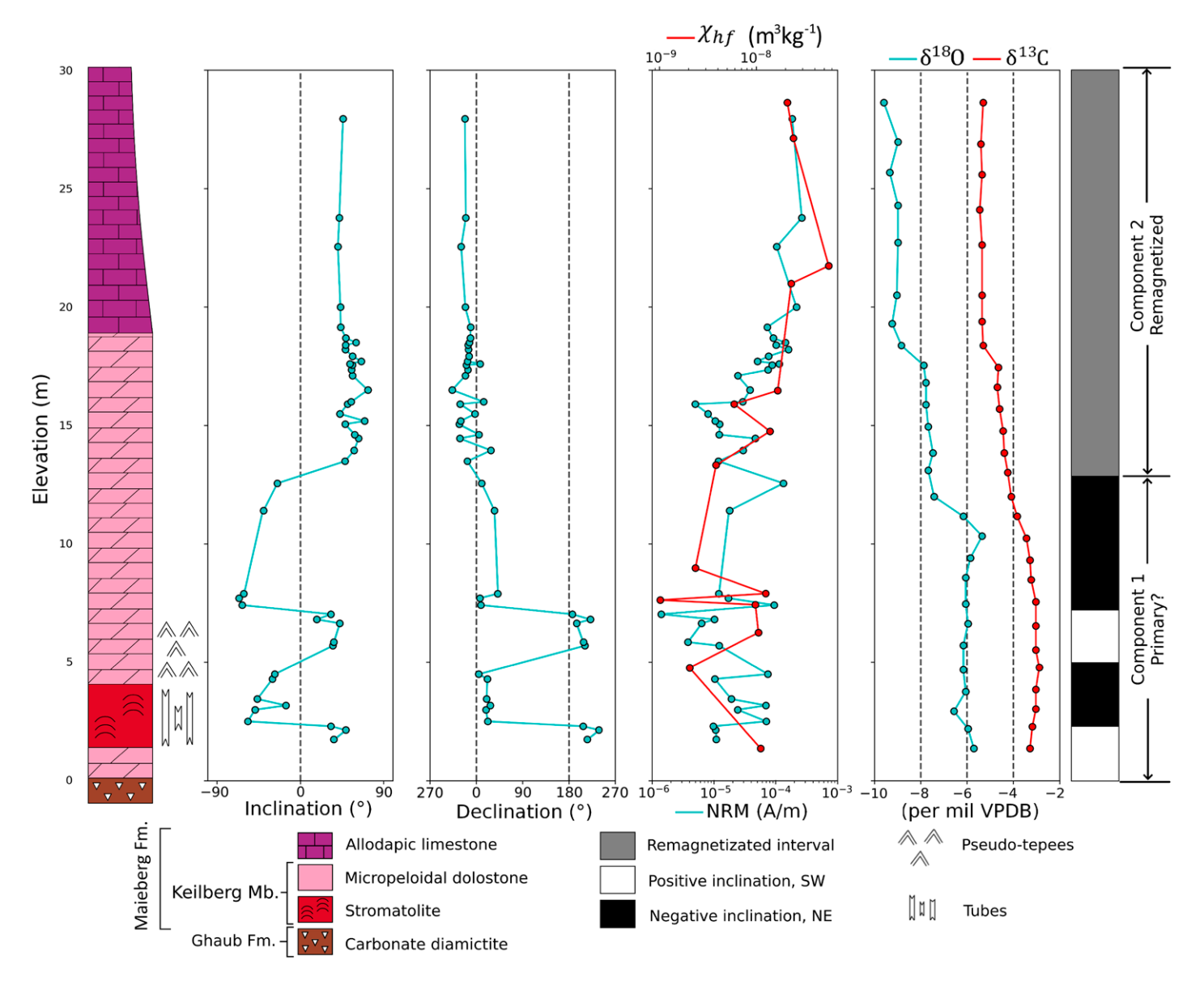


Figure 4. Hoanib shelf stratigraphy and measured mass-normalized bulk susceptibility and remanent magnetization data. Data from sections A and B are merged, considering the elevation of both in relation to the contact with the diamictites (0 m). Carbon/oxygen isotopic curves from Hoffman et al. (1998) and Halverson et al. (2002) are also shown. The magnetostratigraphy is separated into two intervals, where the  $C_1$  component is observed at the lower interval and  $C_2$  in the upper.

directions stem exclusively from one side of the fold (section A). This introduces an additional source of bias to the test. As a result, we classified the  $C_1$  fold test result as inconclusive. In contrast, the directions of the  $C_2$  component deviate significantly from the fold hinge line, which establishes an optimal scenario for the fold test. In this instance, the  $\tau_1$  magnitude reaches its peak within an unfolding range of -10% to 2% (Fig. 6), which unequivocally indicates that magnetization occurred after folding, and thereby yields a negative test result.

#### 4.2. Magnetic Mineralogy

Hysteresis loops show that the ferromagnetic contribution is very small in all of our samples. This is consistent with the recorded intensity of the prior NRM measurements, which demonstrated similarly low values. Most curves prominently exhibit a significant influence from paramagnetic minerals, especially in  $C_2$ -bearing samples. These paramagnetic minerals, as we will elucidate later, are primarily attributed to clays and micas found within these carbonate samples.

Notably, samples carrying the  $C_1$  component display hysteresis loops characterized by a particularly narrower waist and weaker remanence than samples bearing the  $C_2$  component, where a wider waist is often observed (e.g., NA-7A in Fig. 7). The distinctive hysteresis loop configuration referred to as "wasp-waisted geometry," which is commonly encountered in remagnetized Paleozoic carbonate rocks and considered a characteristic "fingerprint" of remagnetization (e.g., Jackson, 1990), was not observed.

Remagnetized and non-remagnetized carbonate formations typically exhibit distinctive mag-

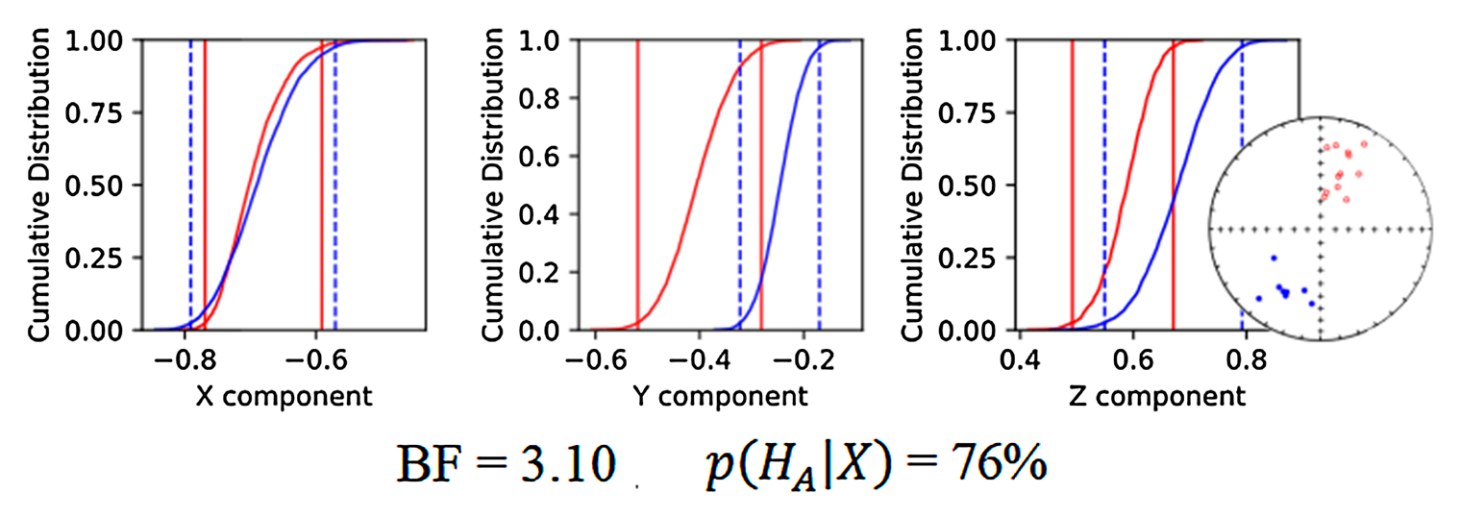


Figure 5.  $C_1$  component reversal test. Cumulative distributions of the Cartesian coordinates of pseudo-sample means taken from the set of directions (blue—reverse polarity directions; red—normal polarity directions) are shown in the stereogram on the right (bootstrap approach). The range containing 95% of each set of components is represented by the vertical lines on the graph. Because the confidence limits of the two datasets overlap in the three components, the averages of the normal and reverse polarities cannot be distinguished at a 95% confidence level.  $C_1$  passes the bootstrap reverse test. Also indicated below are the parameters obtained through the Bayesian reversal test. The numerical result of the test gives a Bayes Factor (BF) of 3.10 and a probability of the sets of directions having the same common mean,  $p(H_A|X)$ , of 76%, which corresponds to a test with positive support.

netic characteristics, as outlined by Jackson and Swanson-Hysell (2012). Among these attributes, a notable one pertains to the Day diagram (Day et al., 1977), where remagnetized carbonates conventionally cluster around the vicinity of the mixing curve encompassing SD to superparamagnetic (SP) particles with a 10 nm threshold (Dunlop, 2002b; Jackson and Swanson-Hysell, 2012). It's intriguing to observe that all of our sample set diverges from the established domain of remagnetized carbonates. Both samples displaying  $C_1$  and  $C_2$  components scatter along with the theoretical mixing curve that represents SD/pseudo-single domain (PSD)/multi-domain (MD) magnetite in the "primary region" of the diagram (Fig. 8). This distribution implies a mixture involving populations of more coercive SD/ PSD magnetite along with less coercive PSD/ MD magnetite, if homogeneous composition and internal stress states are assumed (Dunlop and Özdemir, 1997).

The results obtained from IRM acquisition curves demonstrated consistent patterns for both sample groups. Samples carrying the  $C_1$  and  $C_2$  components displayed near-complete IRM saturation at values below 300 mT, which indicates the dominance of magnetite as the main magnetic mineral (Fig. 7). The IRM unmixing models applied to both component-bearing samples exhibited striking similarity (Fig. 7). The optimal fit to the model was consistently achieved through a combination of two components: one characterized by lower coercivity (ranging from 24.0 mT to 38.8 mT) and a relatively smaller amplitude within the coercivity spectra,

and another characterized by higher coercivity (ranging from 74.2 mT to 92.9 mT) with a larger amplitude. The parameters derived from the two-component IRM unmixing models (Table 3) exhibit reasonable agreement with the established values for coarse detrital magnetite and fine, highly coercive magnetite, as documented by Egli (2003, 2004).

In the context of FORC diagrams, samples containing the  $C_1$  component exhibit patterns characteristic of PSD magnetite. This is evident in the presence of a dispersion along both the coercivity axis  $(B_c)$  and the interaction axis  $(B_u)$ , which results in an approximately triangular configuration (as observed in NA-3E, Fig. 7). Conversely, for samples with the  $C_2$  component (such as NA-7A and NA-8D, Fig. 7), a noticeable shift is discernible from the primary peak of the FORC distribution toward higher  $B_c$  values. Often, two peaks are observed—one at the origin, and the other shifted in  $B_c \sim 50$  mT. Drawing parallels with micromagnetic and experimental models of FORC diagrams arising from the interplay between SD and PSD grains (e.g., Carvallo et al., 2006), we interpret that these observations align coherently with a hybrid composition comprising SD and PSD grains within the remagnetized samples  $(C_2)$ . Conversely, samples interpreted as carrying  $C_1$  are characterized by a predominantly PSD grain population.

#### 4.3. X-Ray Diffraction

In XRD analyses, all samples bearing the  $C_2$  component exhibit a heightened presence of ter-

rigenous minerals in comparison to the samples carrying the  $C_1$ . Remarkably, the intensity peaks linked to illite are markedly more prominent in the  $C_2$ -bearing samples, and are often absent in samples containing the  $C_1$  (Fig. 9). This is consistent with the overall increase in  $\chi_{hf}$  upward in the stratigraphic section. The broader paragenesis established through XRD for our Maieberg samples encompasses calcite, dolomite, quartz, mica (potentially detrital in origin), and potassium feldspar. Peaks indicative of chlorite and smectite were not detected in our observations. Together, this assemblage is indicative of a sub-greenschist facies and low metamorphic conditions.

#### 4.4. Scanning Electron Microscopy

SEM examination of carbonate samples bearing the  $C_1$  component indicates the presence of a relatively modest quantity of terrigenous minerals, including quartz, clays, and micas, dispersed within the carbonate matrix (Fig. 10A). These samples also exhibit distinct magnetite particles of relatively larger dimensions ( $\sim$ 2–10  $\mu$ m) with well-defined boundaries, dispersed and isolated within the carbonate matrix, which imply a likely detrital origin. In contrast, samples carrying the  $C_2$  display a notably higher amount of terrigenous minerals, particularly micas and clays (Fig. 10). In this context, occurrences of magnetite particles of such dimensions are less frequent within the matrix. Instead, finer magnetite grains (<2 µm) are frequently observed, often

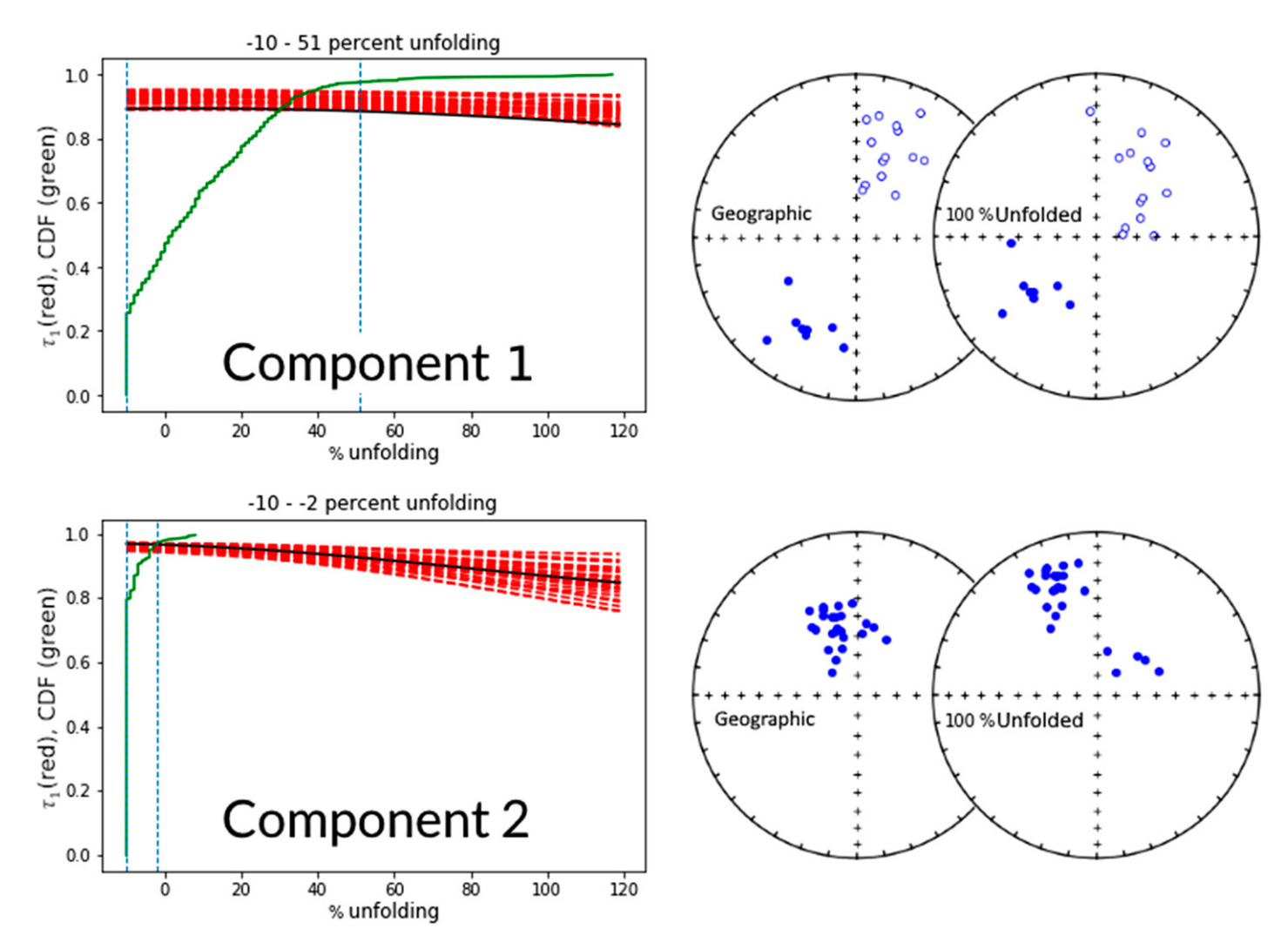


Figure 6. Fold test on  $C_1$  and  $C_2$  components. (Left) Results of the unfolding; dashed red lines are the trend curves of the orientation matrix maximum eigenvalues  $(\tau_1)$ , obtained from pseudo-samples representative of the distribution of the component directions as the layer is unfolded (directions are adjusted for a slope increment of -10% to 110%); the curve of the cumulative distribution of  $\tau_1$  is marked in green; the vertical dashed blue lines are the 95% confidence limits of the cumulative distribution of  $\tau_1$ . (Right) Equal-area projections of the component directions before unfolding (0% unfolding) and after unfolding (100% unfolding).  $C_1$  presents a test interpreted as inconclusive, and  $C_2$  has a negative test.

in association with clay minerals or micas (Fig. 10C).

It is pertinent to highlight that these observations are in concordance with the outcomes from investigations of rock magnetism, which propose the existence of two distinct magnetite populations in these rocks. The first population consists of larger, less coercive magnetite, presumably exhibiting a PSD/MD structure (Figs. 8 and 10), and is more prominent in the carbonate matrix of samples bearing the  $C_1$  component. The second population consists of finer magnetite with an SD/PSD structure (<2  $\mu$ m), which is primarily, but not exclusively, found in conjunction with clays and micas in samples carrying  $C_2$ .

#### 5. DISCUSSION

#### 5.1. $C_1$ Component

The  $C_1$  component exhibits dual polarity with NE negative (SW positive) directions. This component was identified in the lowermost parts of the Keilberg Member dolostones, which are characterized by relatively weaker magnetic remanence ( $10^{-6}$  A/m to  $10^{-4}$  A/m) than the samples from the uppermost parts. Notably, the polarity directions display stratigraphic coherence, with distinct polarities occurring at various stratigraphic levels (Fig. 4).

To validate whether the distributions of both polarities can indeed represent a common mean,

two reversal tests, specifically the bootstrap and Bayesian tests, were conducted. The  $C_1$  component successfully passes both tests, which indicates that it likely samples paleosecular variation and that the distributions are not influenced by secondary components. However, a fold test involving this component yielded inconclusive results. This is primarily due to the limited efficacy of the test arising from the subparallel alignment of the fold hinge with the directions. Additionally, field conditions and sampling led to a situation where 90% of isolated  $C_1$  directions originate from just one side of the fold (section A), which introduces a statistical bias.

Rock magnetic experiments performed on samples containing the  $C_1$  component suggest

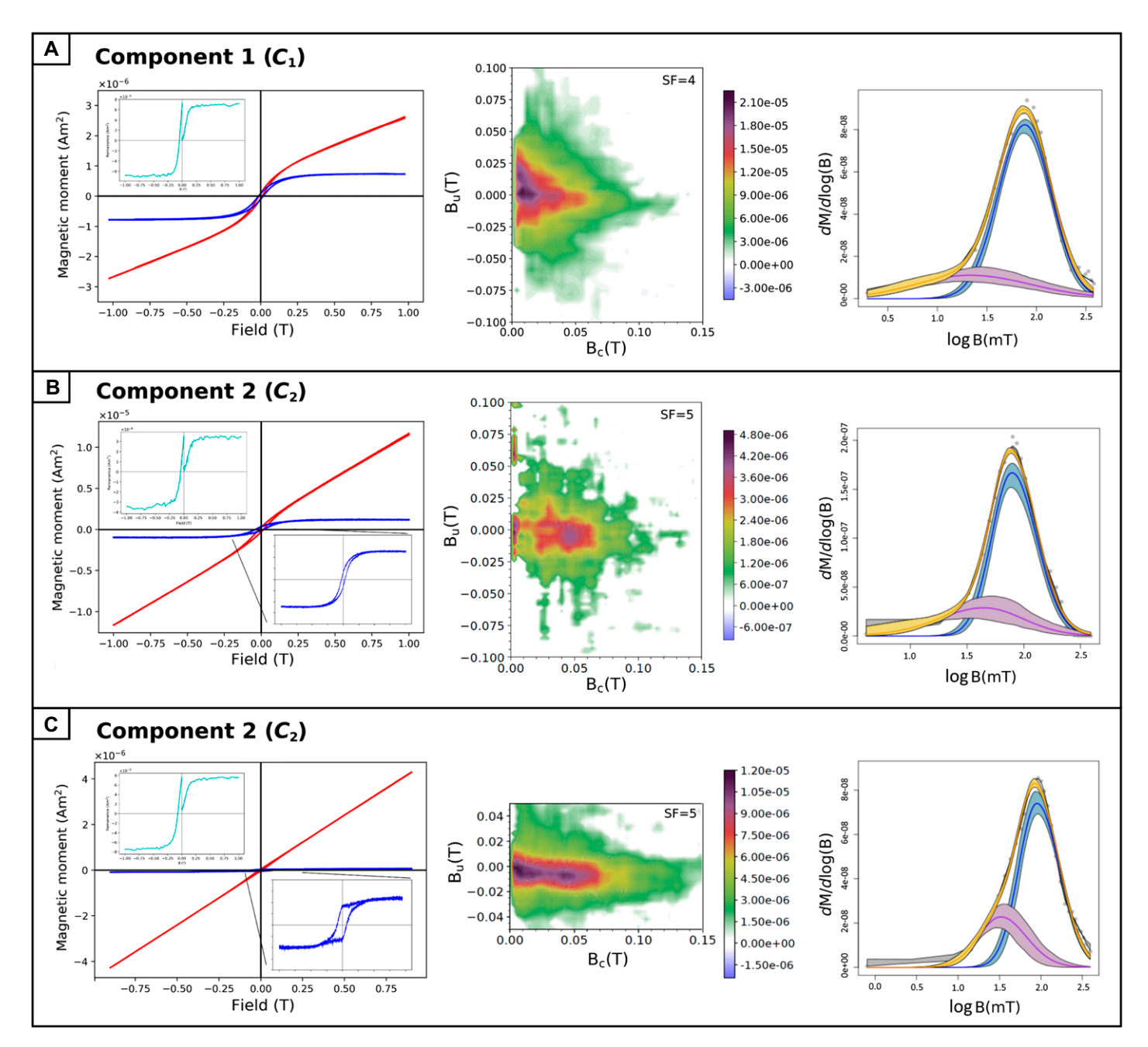


Figure 7. Summary of rock magnetism results for three representative samples: (A) Keilberg dolostone sample NA-3E, (B) Maieberg limestone sample NA-7A, and (C) Maieberg limestone sample NA-8D. Left column shows hysteresis loops where the curve in blue (red) is with (without) paramagnetic correction. Inset in the upper left quadrant of the hysteresis plots is the isothermal remanent magnetization (IRM) and backfield curves. Middle column shows the first-order reversals curve (FORC) diagrams, with the smoothing factor (SF) used in the processing indicated in the upper right. In the column on the right are the coercivity spectra (or gradient acquisition plot, GAP) modeled from the data, where the gray points represent the measurements, the black line is the spline, and the model obtained through the sum of the components is in yellow. IRM component 1 is in purple, and IRM component 2 is in blue. In the latter, the colored area around the lines represents the error associated with the estimates. See text for discussion.

that magnetite predominantly contributes to the remanence in these rocks. The signatures point toward a PSD domain structure, although some grain sizes, observed via SEM, align more closely with an MD structure. X-ray diffractograms and SEM/EDS images of these samples indicate a relatively low presence of terrigenous minerals, particularly clays. Backscattered electron (BSE) images reveal magnetite grains ranging from 2  $\mu m$  to 10  $\mu m$  in size, which feature subangular to subrounded boundaries. These magnetite grains are found isolated

within the carbonate matrix, which suggests a detrital origin.

Considering the existence of reversals, the positive reversal tests, and the mineral phase relationships that suggest a detrital origin for PSD magnetite grains within these rocks, we interpret

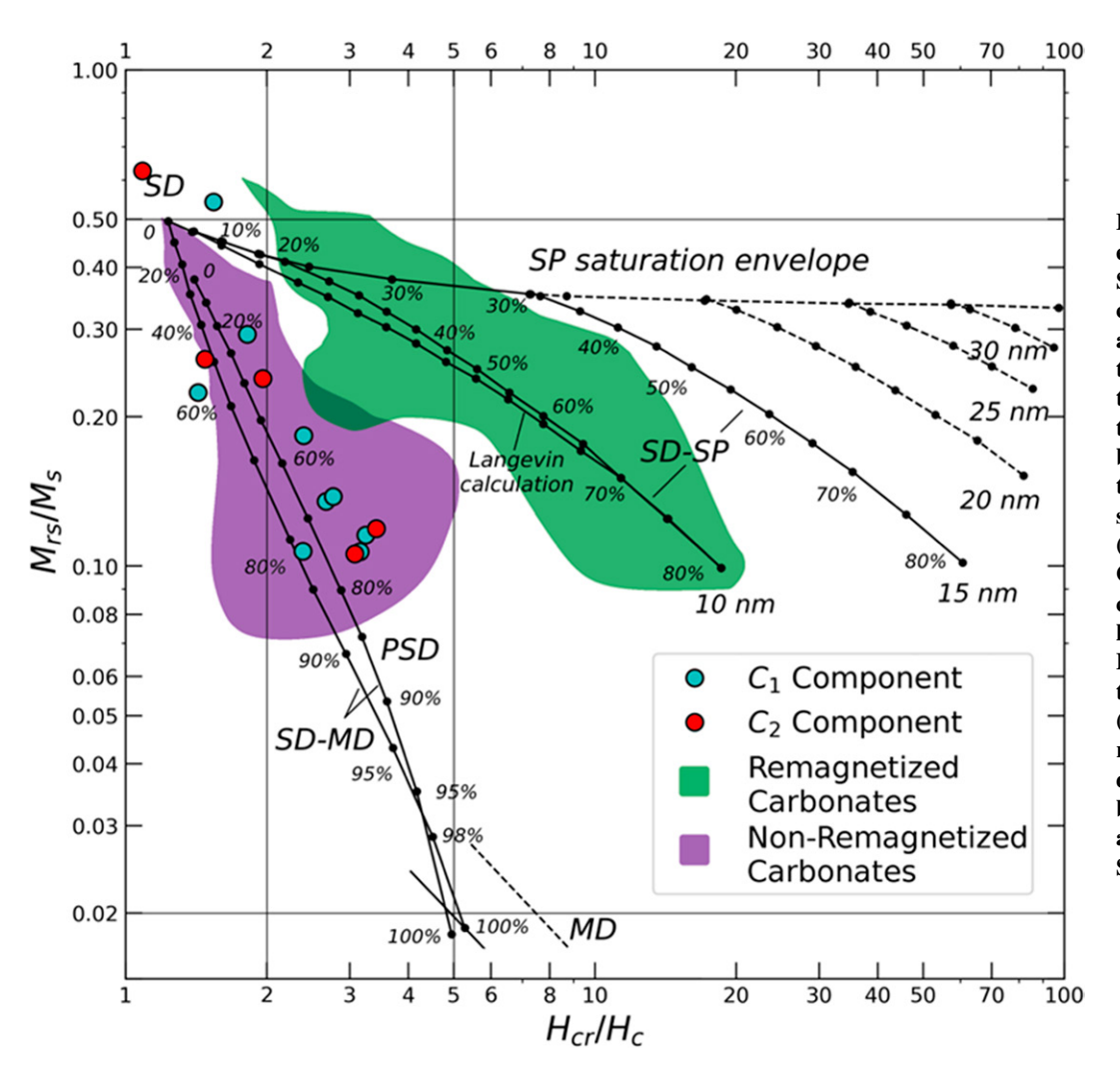


Figure 8. Day diagram (Day et al., 1977; Dunlop, 2002a). Samples that carry the  $C_1$ component are plotted in blue, and the samples that carry the  $C_2$  component in red. Note that no general trend distinguishes the two groups; both are distributed along single domain-pseudosingle domain-multi-domain (SD-PSD-MD) mixing curve. Green (purple) regions indicate the zones of published parameters hysteresis Phanerozoic carbonates interpreted remagnetized as (non-remagnetized). These regions were approximately drawn with the data compiled by Dunlop (2002b) and Jackson and Swanson-Hysell (2012). SP—superparamagnetic.

the  $C_1$  component as potentially representing a primary magnetization of depositional origin acquired during (or close to) rock formation.

#### 5.2. $C_2$ Component

The  $C_2$  component is characterized by a positive NNW direction of relatively stronger intensity as compared to  $C_1$  ( $10^{-5}$  A/m to  $5 \cdot 10^{-4}$  A/m). It was observed stratigraphically above the  $C_1$ 

interval in both Keilberg dolostone and Maieberg limestone. The  $C_2$  fold test is negative and indicates that this magnetization was acquired after the folding event (at ca. 580–570 Ma).

Rock magnetic experiments with samples that carry this component show that magnetite is the main magnetic mineral, and is characterized by features suggestive of an SD to PSD domain structure. X-ray diffractograms highlight a notably higher concentration of terrigenous minerals,

particularly micas and clays, in  $C_2$ -bearing samples than those containing  $C_1$ . BSE imaging corroborates this observation, revealing finer magnetite grains generally  $<2 \,\mu m$  in size, which are closely associated with micas and clays rather than dispersed within the carbonate matrix.

Furthermore, the variation in  $\chi_{hf}$  ( $\geq$ 700 mT) across the stratigraphy, which primarily reflects the concentration of paramagnetic minerals (micas and clays), roughly follows the fluctuation in NRM intensity. This suggests a connection between the clay-rich fraction and the concentration of ferromagnetic (s.l.) minerals. In conclusion, the  $C_2$  component is interpreted as arising from a remagnetization event after folding, originating from fine and stable SD to PSD ( $<2 \mu m$ ) magnetite, which is likely of authigenic origin.

### TABLE 3. COMPONENT PARAMETERS IN THE COERCIVITY ISOTHERMAL REMANENT MAGNETIZATION (IRM) SPECTRA

Sample		IRM com	ponent 1		IRM component 2					
	$B_h$	DP	p	s	$B_h$	DP	р	s		
NA-1H	23.6	2.83	0.16	0.77	76.7	1.74	0.89	0.93		
NA-3E	24.0	3.83	0.12	1.09	75.6	1.84	0.91	0.99		
NA-4E	38.2	2.27	0.21	1.03	80.2	1.66	086	0.96		
NA-5C	30.2	2.70	0.18	1.06	77.6	1.79	0.88	0.99		
NA-6I	34.0	1.71	0.17	1.05	82.8	1.77	0.94	1.02		
NA-7A	38.8	2.41	0.15	0.93	84.1	1.57	0.86	1.10		
NA-8D	29.5	1.99	0.20	1.04	92.9	1.83	0.91	1.05		
NA-10H	30.8	2.77	0.23	0.88	74.2	1.70	0.81	0.98		

*Note:*  $B_n$ —mean coercivity of an individual grain population; DP—dispersion parameter; p—proportion factor; s—skewness parameter.

### 5.3. Late Neoproterozoic Paleomagnetism of Congo-São Francisco Craton

The pole derived from the  $C_1$  (CSF1; CSF—Congo–São Francisco) data, which incorpo-

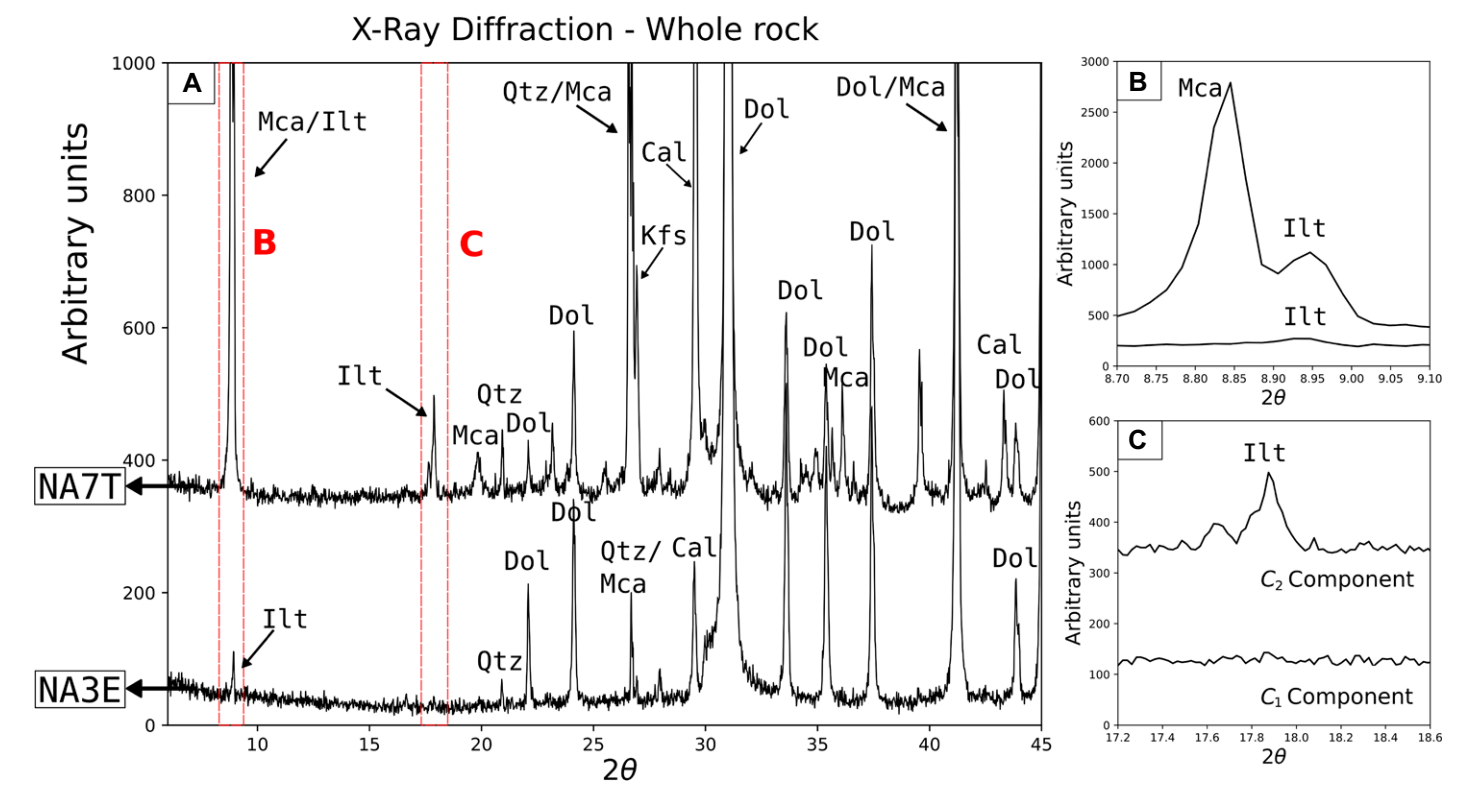


Figure 9. (A) X-ray diffraction of two representative samples of the Maieberg carbonates. Sample NA-3E is a sample that carries  $C_1$  component (primary?), and sample NA-7T carries  $C_2$  component (remagnetized). (B) Zoomed-in view of one of the peaks of illite and mica. Note the intense peak in the NA-7T sample (top line) while the NA-3E sample (bottom line) shows practically no peaks. (C) Zoomed-in view of one of the illite peaks, which highlights the well-marked peak in the NA-7T sample (top line) and its absence in the NA-3E sample (bottom line). Cal—calcite; Dol—dolomite; Ilt—illite; Kfs—potassium feldspar; Mca—mica; Qtz—quartz.

rates both polarities, in African coordinates falls at a longitude  $[\varphi(p)]$  of 312.1°E, latitude  $[\lambda(p)]$  of 45.4°S, dp of 6.9°, and dm of 10.1° (Fig. 11; Table 4). This pole does not coincide with any younger Paleozoic pole (e.g., Torsvik et al., 2012).

The Kaoko Belt, which is adjacent to the Maieberg carbonates, had its main tectonometamorphic phase in response to the obduction of the so-called coastal terrains of the Damara Orogenic System toward the western margin of the Congo craton ca. 580-570 Ma (Passchier et al., 2002; Goscombe et al., 2005). This timeframe corresponds well with the positioning of the  $C_1$ pole in the West Gondwana apparent polar wander path (APWP; Rapalini, 2008; Trindade et al., 2006; Tohver et al., 2006) on a region well-determined by a set of  $\sim$ 580 poles of an almost completely assembled West Gondwana. This observation implies the possibility of a syntectonic remagnetization event (since 600 Ma), which was potentially influenced by thermal effects arising from the Kaoko thermal metamorphism.

However, some challenges need to be addressed in this interpretation:

(1) Congo's motion constrained by the poles of the Mbozi Complex (743 Ma; Meert et al.,

1995), the Nola dikes metadolerites (571 Ma; Moloto-A-Kenguemba et al., 2008), and the Sinyai metadolerites (547 Ma; Meert and Van der Voo, 1996) agree with the position of southern Congo at a paleolatitude of  $\sim 30^{\circ}$  ca. 630–600 Ma as determined by the  $C_1$  mean inclination (see fig. 14.2 of Trindade et al., 2021, and fig. 6 of Li et al., 2013).

(2) The suggestion of a thermally induced remagnetization of the  $C_1$  component presents physical difficulties. Explaining how the regional metamorphism affected closely spaced stratigraphic intervals at different times, leading to symmetrical reversals along the stratigraphic column, requires additional unknown mechanisms. Furthermore, this explanation must also address the differing effects of thermomagnetic resetting in the  $C_1$  and  $C_2$  stratigraphic intervals. Other processes, such as chemical or late diagenesis remagnetization, cannot be ruled out; however, our rock magnetism and electrooptical analyses point to characteristics that are more consistent with a remanence carried by detrital particles rather than authigenic particles for  $C_1$ -bearing rocks.

(3) Analyzing the metamorphic and isograd field map along the Kaoko and Damara belts,

synthesized from numerous publications by Goscombe et al. (2018), reveals that the region sampled experiences low-grade metamorphism that is between anchimetamorphism and diagenesis/ anadiagenesis. The mineral paragenesis identified in these rocks (presence of illite + K-feldspar, and absence of chlorite) supports this observation. Consequently, the dominant role of thermal metamorphism effects only in the reacquisition of remanence in these rocks seems unlikely.

(4) The  $C_1$  pole derived from the Keilberg dolostone falls close to the poles associated with the Nola dikes and Sinyai metadolerite (Fig. 11B). Although this proximity may lead to concerns about potential remagnetization, this arrangement of pole positions also aligns well with the established movement pattern from the Congo (Trindade et al., 2021).

In summary, the complex geological context suggests that while a remagnetization event linked to thermal effects is a possibility, mainly due to the position of  $C_1$  to younger poles and the coherence of this position with the age of the peak of regional metamorphism, physical challenges make it difficult to fully accept this explanation. The magnetic and nonmagnetic mineralogical characteristics of  $C_1$ -bearing rocks, the

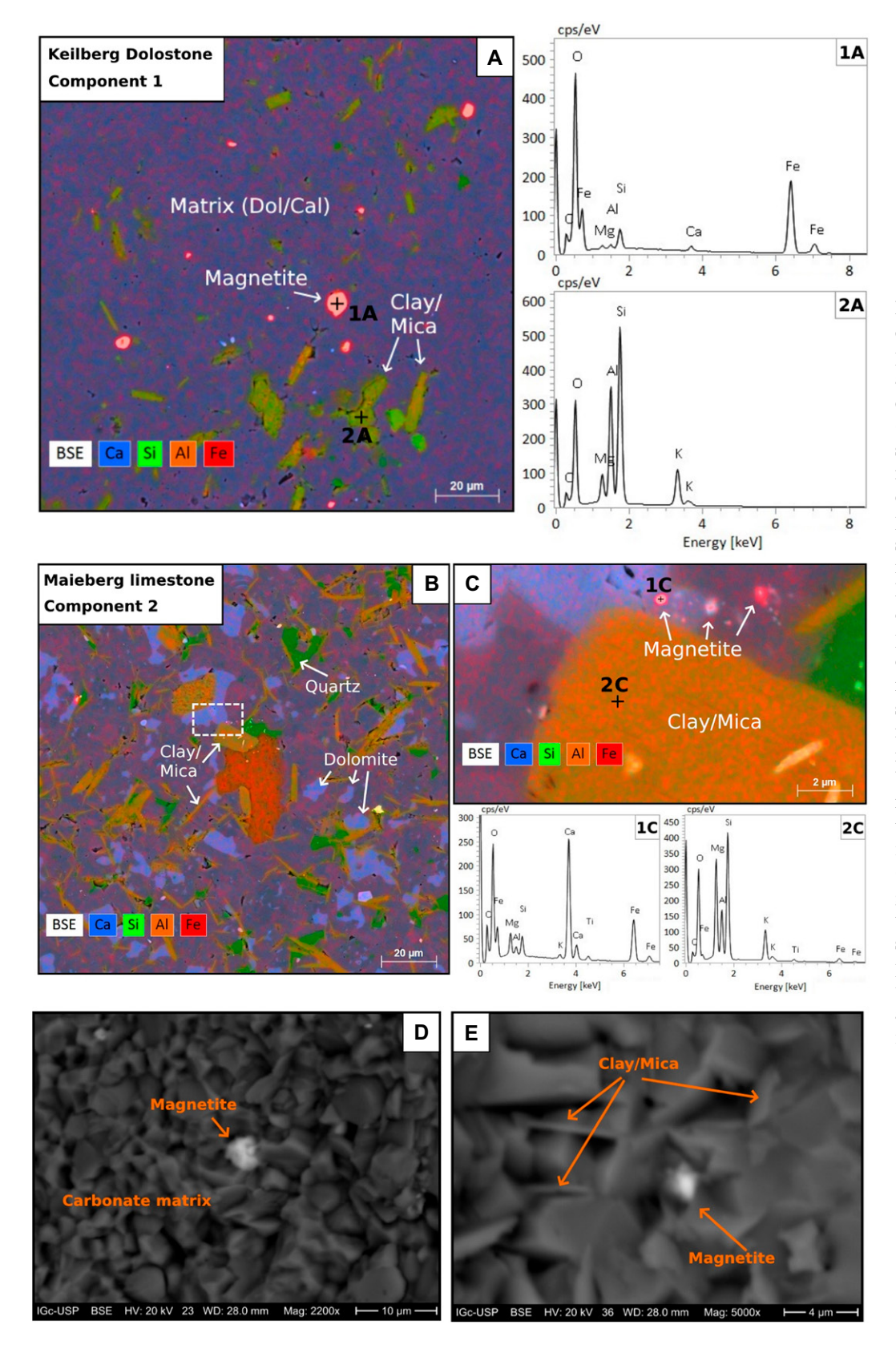


Figure 10. (A) Backscattered electrons (BSE) from a  $C_1$  component carrier sample (NA-2H) and elemental map obtained by energy-dispersive spectroscopy (EDS). On the right are the EDS spectra of the targets indicated in the image. Cal-calcite; Doldolomite. (B) BSE of a  $C_2$  component (remagnetized?) carrier sample (NA-7Q) and elemental map obtained through EDS. Note the much more micaceous/ clayey matrix compared to the previous sample. (C) Zoom indicated by white rectangular box in part B. Below are the EDS spectra of the targets indicated in the image. Dark blue matrix is composed of calcite, and light blue indicates dolomite. (D) BSE image of a magnetite grain amid the carbonate matrix in a nonremagnetized dolostone sample. (E) BSE image of a magnetite grain in a clay/mica-rich matrix in a remagnetized limestone sample. Small red "spots" in parts A, B, and C interdigitated with the blue in the matrix are analysis artifacts and do not represent iron detection.

motion pattern of the Congo craton, and the metamorphic characteristics of the area sampled contribute to the evidence of the overall hypothesis of primary magnetization. So, although we recognize that this is still an open question, for now, we prefer the latter interpretation. If  $C_1$  is accepted as a primary pole, when contrasting the newly established APWP for the Congo-São Francisco craton, anchored

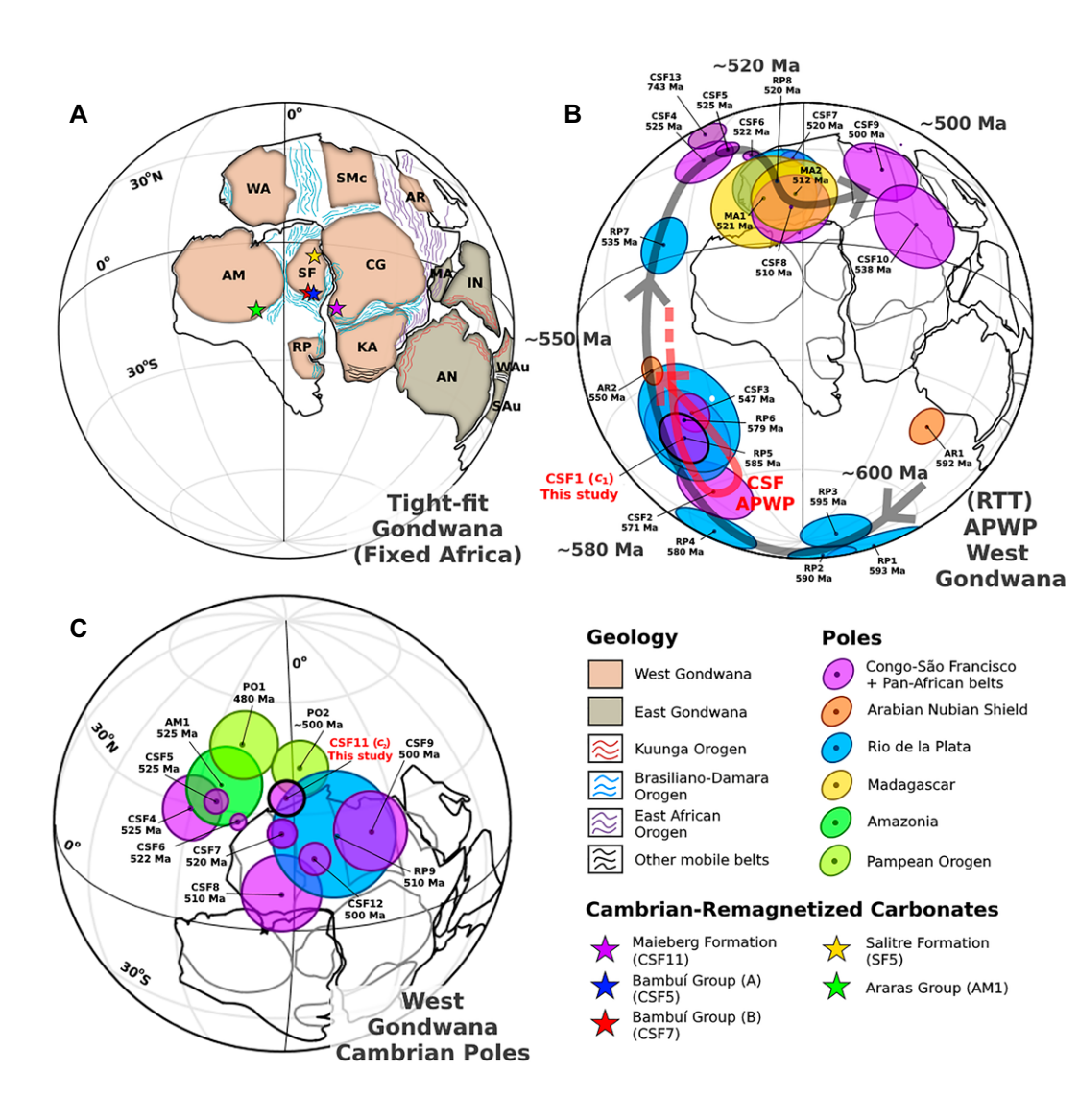


Figure 11. West Gondwana apparent polar wander path (APWP) and the positioning of the Maieberg poles. (A) Reconstruction of Gondwana with fixed Africa ("tight fit") using the rotations of Reeves et al. (2004) and Trindade et al. (2006). Geology and tectonic units are after Gray et al. (2008). AM-Amazonia; RP-Rio de la Plata; SF-São Francisco; WA-West Africa; SMc-Sahara metacraton; CG-Congo; CSF-Congo-São Francisco; KA-Kalahari: AR-Arabia Nubian Shield; MA-Madagascar; IN-Indian Shield; AN-East Antarctic Shield; WAu-West Australia; SAu-South Australia. Stars represent West Gondwana carbonate units with verified Cambrian remagnetizations. (B) Rapalini-Tohver-Trindade (RTT) APWP of West Gondwana (Rapalini, 2008; Tohver et al., 2006; Trindade et al., 2006) and the positioning of the  $C_1$  pole (CSF1). Red line indicates the APWP of Congo-São Francisco inferred with the new  $C_1$  pole. (C) Cambrian reference poles of West Gondwana, remagnetization poles, and the positioning of  $C_2$  pole (CSF11). See text for discussion.

by the  $C_1$  pole, with the APWP of the Rio de la Plata craton, it becomes evident that these geological blocks maintained distinct tectonic histories until ca. 580 Ma. At this point, their respective APWPs coincide. This last finding, which is based on paleomagnetic data, matches reasonably well with tectonic models that rely on geochronological and metamorphic evidence (Basei et al., 2018; Goscombe et al., 2005; Gray et al., 2008). We note that recently, Cukjati et al. (2023) proposed an alternative pre-580 Ma path for Rio de la Plata. However, our inferences of independent kinematics before that time remain valid.

When compared to other poles associated with Gondwana, the position of the Dokhan volcanics pole of the Arabian-Nubian Shield, dated at ca. 593 Ma (Nairn et al., 1987), continues to suggest that this block maintained its status as an independent tectonic unit until ca. 550 Ma. This observation corresponds with findings

from previous research (Rapalini, 2018; Antonio et al., 2021), although the possibility of an even earlier connection cannot be ruled out due to the lack of available paleomagnetic data. For example, Cukjati et al. (2023) interpret that these blocks were already amalgamated by 615 Ma.

Although there is plenty of geological evidence for a relatively late (555–505 Ma) collision of the Kalahari craton with the Congo craton (e.g., Coward, 1981; Miller, 1983; Porada, 1983; Gray et al., 2008), the tectonic history between the southern Congo craton and the Kalahari region remains poorly constrained from a paleomagnetic perspective. This limitation arises from the scarcity of reliable late Neoproterozoic paleomagnetic data for the Kalahari and Congo cratons (Evans et al., 2021).

Recently, the examination of paleomagnetic poles within the context of Gondwana has sparked discussions concerning notably high apparent plate velocities during the Ediacaran and Early Cambrian periods (Robert et al., 2017; Antonio et al., 2021; Cukjati et al., 2023). To explain this phenomenon, the concept of true polar wander (TPW) has been put forth. TPW involves rapid shifts in the orientation of the lithosphere and mantle relative to the rotation axis, which results from uneven distribution of mass within Earth (Kirschvink et al., 2005: McCausland et al., 2007; Mitchell et al., 2011; Robert et al., 2017). By considering the  $C_1$ / Keilberg (635 Ma) and Nola (571 Ma) paleomagnetic poles, one can calculate an apparent angular drift rate of 0.27°/m.y. for the Congo-São Francisco craton from the early to mid-Ediacaran, which implies plate velocities similar to those of modern times. However, it is important to emphasize that this discussion remains preliminary in relation to this craton primarily due to the lack of highly reliable paleomagnetic poles from this period. Consequently, while

TABLE 4. SELECTED GONDWANAN PALEOMAGNETIC POLES

TABLE 4. SELECTED GONDWANAN PALEOMAGNETIC POLES													
Code	Unit	Lithology	φ <b>(s)</b>	$\lambda(s)$	D	I	$\alpha_{95}$	k	A <sub>95</sub> (dp/dm)	φ <b>(p)</b>	λ <b>(p)</b>	Age (Ma)	Reference
Congo-São Francisco craton ± Pan-African belts													
CSF1 CSF2	Meieberg Formation $C_1$ Nola Metadolerite	Sed. Metam.	14.0 16	-19.3 3.5	47.69 26.7	-52.82 -11.2	7.26 10.5	21.15 24.01	6.95/10.06 5.0/10.0	312.0 304.8	-45.37 -61.8	ca. 630 571	This study Moloto-A-Kenguemba et al. (2008)
CSF3	Sinyai Metadolerite	Metam.	37.05	0.2	241	20	5	20	3.0/5.0	319	-29	547	Meert and Van der Voo (1996)
CSF4 CSF5	Itabaiana dikes Bambuí + Salitre (remagnetized)	lgn. Sed.	-35.5 -41	-7.2 -12.5	168 5.8	-64 63.2	5.7 2.9	46 105.1	7.3 3	314.6 322	34.9 32	525 525	Trindade et al. (2006) Trindade et al. (2004)
CSF6 CSF7 CSF8	Ntonya Ring Bambuí B Juiz de Fora Complex	Metam. Sed. Metam.	35.2 -41 -42.5	-15.2 -12.5 -21.5	311.3 25.6 2.9	42.8 68.3 75.4	1.9 1.6 6.4	1054 247.5 17.9	1.8 3 10.3	345 331 320.1	28 15 4.2	522 520 510	Briden (1968) Trindade et al. (2004) D'Agrella-Filho et al.
CSF9	Piquete Formation	Metam.	-42.5	-21.5	60	68	10		10	347	-1	500	(2004) D'Agrella-Filho et al.
CSF10 CSF11	Monteiro dikes Maieberg Formation C <sub>2</sub>	lgn. Sed.	-37.06 14.0	-7.8 -19.3	298.5 344.7	-76 53.9	6.8 4.3	25.4 44.0	11.7 4.21/6.01	344.9 358	-18.2 34.32	538 520	(1986) Antonio et al. (2021) This study
CSF12	(remagnetized) Santa Agelica/Venda Nova plutons	lgn.		-20.17	27.84	74.23	4.27	33.15	4.1	332.2	4.7	500	Temporim et al. (2021)
CSF13	Mbozi Complex	lgn.	32.9	-9.3	320	16	9	32	5/9	325.0	46.0	743	Meert et al. (1995)
Arabia Nubian Shield													
AR1 AR2	Dokhan Volcanics Mirbat Sediments	Intr. Sed.	33.6 54.46	26.6 17.05	178.1 69.5	36.8 18.5	9.64 7.2	33.3 46.4	10 3.9/7.5	36.2 321.8	-42.7 -23.3	592 550	Nairn et al. (1987) Kempf et al. (2000)
	a Plata craton												
RP1	Playa Hermosa Formation	Sed.	-34	<b>–</b> 55.5	207.6	27.3	12.4		12.1	183.1	-58.8	593	Rapalini et al. (2015)
RP2 RP3	Villa Monica Formation Campo Alegre Formation	Sed. Intr.	-37.3 -26.5	-59.2 -49.3	43.4 36	-36.3 -40	9.1 10	45 56	8.5 9	198.1 223	-48.8 -57	590 595	Rapalini et al. (2013) D'Agrella-Filho and Pacca (1988)
RP4 RP5	Cerro Largo Formation Los Barrientos	Sed. Sed.	-37.3 -37.8	-59.2 -59	77.3 104.5	-36.3 60.8	12.1 9.3	15 23	11 12.9	217.4 253.9	-24.8 -16.2	580 585	Rapalini et al. (2013) Rapalini (2006)
RP6	Claystone Sierra de las Animas Complex	Intr.	-34.6	-55.3	108	-60.6	10.4	20	14.9	258.9	-12.2	579	Rapalini et al. (2015)
RP7 RP8 RP9	Olavarría Formation Cerro Negro Formation Sierra de las Animas Complex (remagnetized)	Sed. Sed. Intr.	-37.3 -37.3 -34.6	-59.2 -59.2 -55.3	349.3 28.7 44.5	49.9 56.1 58	7 9.5 18.1	37 15 10	7.5 11.5 18.1	289.9 323 338.1	21.7 11.8 5.9	580 520 510	Rapalini et al. (2013) Rapalini et al. (2013) Sánchez-Bettucci and Rapalini (2002)
Madaga					.=.								
MA1	Madagascar Virgation Zone	Metam.	47.3	-18.5	271	54	10.1	14.4	14.2	352.6	-6.7	521	Meert et al. (2003)
MA2	Carion Granite	Metam.	47.5	-18.7	278	62	11	27	13/17	1	-6.9	512	Meert et al. (2001)
Amazor AM1	<u>nia craton</u> Araras Group (remagnetized)	Sed.	-58.0	-16.0	25.7	55.4	7	28.9	10	327	34	525	Trindade et al. (2003)
Pampean Orogen													
PO1	La Pedrera Fm.	Sed.	-65.2 65.4	-25.1	35	25.7	8.9	24.6	8.8	340.4	38.3	480	Rodríguez Piceda et al. (2018)
PO2	Campanario Fm.	Sed.	-65.4	-24.1	50.2	32.8	8.3		7	346.5	23.6	500	Franceschinis et al. (2020)

Note:  $\varphi(s)$  and  $\lambda(s)$ —site longitude and latitude; D—declination; I—inclination,  $\alpha_{95}$ ,  $A_{95}$ —angle of the 95% confidence cone; k—precision parameter;  $\varphi(p)$  and  $\lambda(p)$ —pole longitude and latitude; dp and dm—pole confidence ellipse semi-axis; Sed.—sedimentary; Intr.—intrusive; Ign.—igneous; Metam.—metamorphic.

these findings do not rule out the occurrence of TPW-type events, the overall assessment remains tentative.

With all of that said, we recognize the  $C_1$  pole as being of medium quality (Q = 4, R = 4; Van der Voo, 1990; Meert et al., 2020) and fitting as a B-grade pole ("poles that are judged to be indicative or suggestive of reliability, but are lacking in one or more of the quality criteria," Evans et al., 2021). Therefore, we suggest caution in using this pole in reconstructions and other paleogeographical inferences. In the future, more regionalized studies, with a greater number of samples and better-determined stability tests, should confirm or invalidate these hypotheses.

## **5.4.** Paleogeography of Cap Carbonates and Glacial Deposits

The  $C_1$  component offers constraints on the sedimentation of Maieberg cap carbonates, and provides a paleolatitude of  $33.3^{\circ} \pm 3.2^{\circ}$ . Assuming a negligible temporal interval between the end of glacial sedimentation and the onset of carbonate precipitation—which is indicated by the distinct and smooth transition between the diamictite and the cap dolostone that is devoid of features such as karst development, sediment lag, or clear indications of exposure or substantial hiatus (Hoffman, 2002)—this paleolatitude serves as an initial quantitative estimation of the

deposition paleolatitude of the Ghaub glaciogenic deposits.

The data imply that the ice sheets experienced a minimum advance to  $\sim\!30^\circ$  latitude at ca. 635 Ma. According to the energy balance model of Budyko-Sellers (Budyko, 1969; Sellers, 1969), this advance is more than sufficient to trigger an uncontrolled migration of the ice line toward equatorial latitudes due to the influence of icealbedo instability. The current paleomagnetic data reveal that continental landmasses and glacial sediments are widely distributed across different paleolatitudes (Evans and Raub, 2011). These sediments span from  $\sim\!60^\circ$  latitudes down to equatorial latitudes. Considering the spectrum

of estimated paleolatitudes for these sediments both after and during the Marinoan glaciation, several indications strongly support the notion that glacial action widely influenced Earth's surface during this period, which is in line with the postulations of the SBE theory.

From a sedimentological perspective, our derived paleolatitude of  $\sim 33^{\circ}$  for the Keilberg dolostones appears notably elevated. Ancient nonskeletal carbonates exhibit consistency with both the spatial variation in the carbonate saturation state found in the modern ocean (Jiang et al., 2015) and the temperature-dependent nature of carbonate saturation (Millero, 1979). These carbonates are primarily distributed within a range of  $\sim 35^{\circ}$  from the equator. This would position the Otavi platform in proximity to the outer boundary of this distribution. Nevertheless, it is important to note that cap carbonates diverge from the typical latitudinal patterns exhibited by Phanerozoic chemical carbonates. Cap carbonates manifest wider latitudinal variations, which is a result of the peculiar carbonate saturation state that emerges when an ocean, buffered in its composition, experiences rapid and strong warming following extensive glaciations. Consequently, estimated paleolatitudes for cap carbonates can extend to  $\sim 60^{\circ}$ . The absence of cap carbonates at latitudes exceeding this range is attributed to the paleogeographical limitations posed by the absence of continental masses in such positions during the Cryogenian period (e.g., Li et al., 2013).

The findings of Hoffman and Li (2009) propose a relationship between the thickness of cap dolostones and the paleolatitude at which they were formed. This relationship suggests that thickness increases toward the equator, likely due to factors such as warmer waters, which results in higher carbonate oversaturation. Additionally, since the ice sheets retreated poleward from the equatorial region, areas at lower paleolatitudes would have experienced longer periods of syn-deglacial cap dolostone formation. Consequently, as the Keilberg cap dolostone is one of the best developed in Gondwana in terms of thickness, we would expect a lower paleolatitude.

When examining the distribution of cap dolostone thicknesses based on their inferred paleolatitudes from various paleogeographic models, a prevalent pattern emerges. Most of these cap dolostones exhibit total thicknesses below 15 m, spanning across a wide range of paleolatitudes (Fig. 12). There are instances of thicker cap dolostones that seem to have formed at paleolatitudes lower than 20°, according to the insights provided by paleogeographical models (e.g., Li et al., 2008; Li et al., 2013; Merdith et al., 2021). However, this trend is not exclusive. Interestingly, the Keilberg cap dolostone stands out due to its anomalous thickness if a paleolatitude of 33° is assumed. This also holds true for the paleolatitude estimated for the Keilberg Member across three distinct paleogeographic models, each of which is based on different poles and was determined by different methodological approaches (Fig. 12A).

These observations imply that in addition to the impact of paleolatitude on carbonate oversaturation, other contributing factors have influenced the development of these cap dolostones. Elements such as local alkalinity sources (e.g., Geyman et al., 2022) during the marine transgression of areas previously covered by glaciers, and the variation in sediment accommodation space resulting from local net tectonic subsidence that accumulated during the prolonged glacial period when sedimentation rates were anomalously low, have likely played important roles. For the Maieberg Formation, a combination of favorable conditions seems to have led to an anomalously substantial thickness, even beyond the equatorial belt. Conceivably, the extensive weathering of the underlying carbonate platform introduced considerable alkalinity into the melted glacial water. Simultaneously, the subsiding margin of the Otavi platform created a vast space for sediment accommodation during the glacial epoch (Hoffman et al., 1998), which was marked by reduced sedimentation (Partin and Sadler, 2016). This cumulative interplay likely culminated in the development of the thick syn-glacial and postglacial cap carbonate at the southern edge of the Congo craton. However, it is important to note that other cap dolostones resting on carbonate platforms as alkalinity sources (e.g., Mongolia, Bold et al., 2016) are not as thick as the Keil-

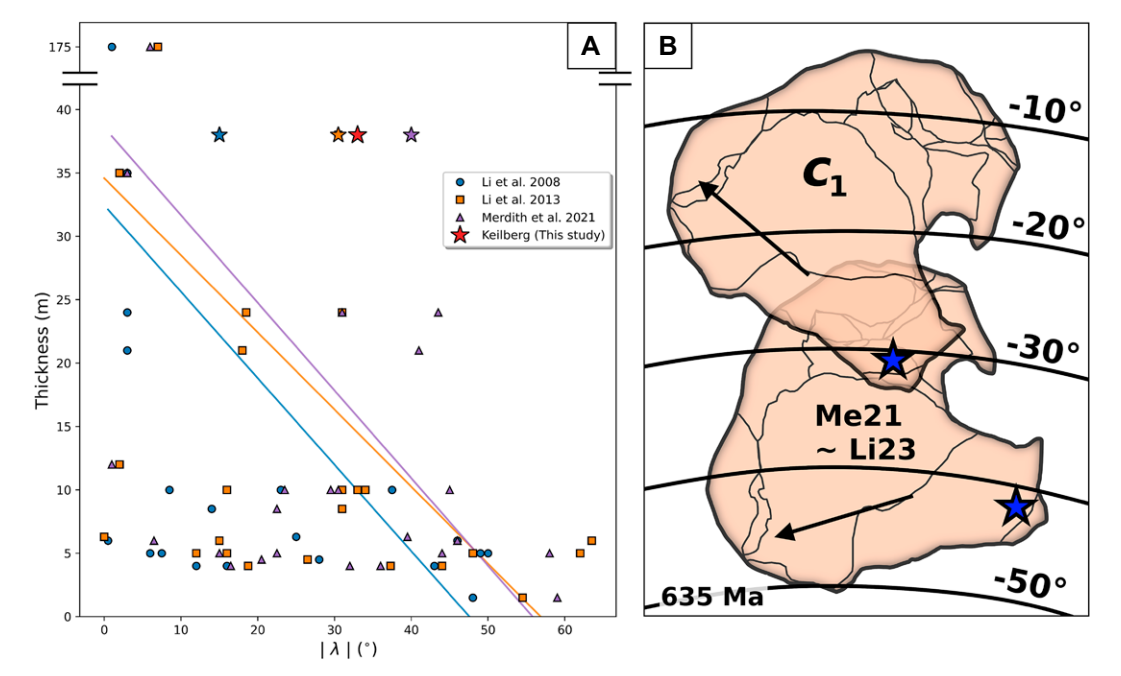


Figure 12. (A) Thickness distribution of Marinoan cap dolostones according to their paleolatitude  $(\lambda)$  estimated in different paleogeographical reconstructions at ca. 635 Ma. The star-shaped dots represent the Keilberg Member. Red indicates the paleolatitude obtained in this study (33.3°). Also shown are the lines adjusted to each data distribution. (B) Comparison between the paleogeographic position of the Congo craton constrained by pole  $C_1$  and recent global paleogeographic reconstructions (Me21-Merdith et al., 2021; Congo in a similar position in Li23—Li et al., 2023) at 635 Ma. Arrow indicates the north direction in its present position; blue star indicates the approxi-

mate location of the Hoanib section (Keilberg Member). Note the lower paleolatitude for the southwestern margin of the Congo craton at ca. 635 Ma constrained by  $C_1$  in comparison to these models.

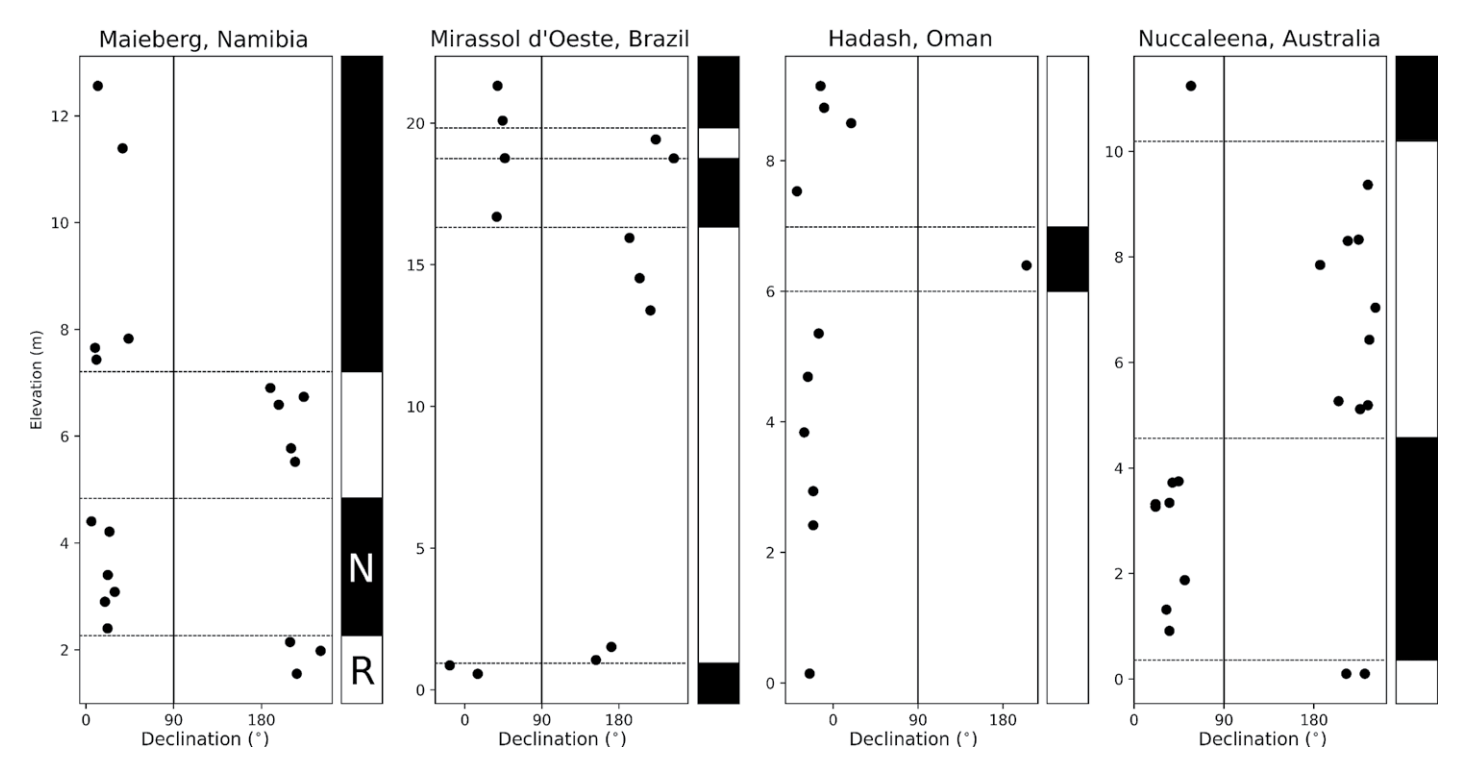


Figure 13. Comparison between magnetostratigraphy in different basal cap carbonates. The elevation of 0 m refers to the contact of carbonates with diamictites. Note the differences in vertical scale among the different sections. Maieberg, Namibia, Hoanib Shelf section (this study); Mirassol d'Oeste, Brazil (Trindade et al., 2003); Hadash, Oman, Jebel Akhdar section (Kilner et al., 2005); Nuccaleena, Australia, Second Plain section, NF02 (Schmidt et al., 2009). N—normal polarity; R—reverse polarity.

berg Member, which places a constraint on this interpretation.

Glacial deposits containing volcanic ash tend to be concentrated in low-latitude regions, typically below <25°, because of the dynamics of ice flow and the accumulation of dust within the net sublimation zone (Li and Pierrehumbert, 2011; Goodman and Pierrehumbert, 2003). In such areas, volcanic ash would be transported by moulin flushes to the underlying ocean, facilitating its deposition of sediment (Goodman and Strom, 2013; Hoffman et al., 2017). Interestingly, the Ghaub glacial deposits themselves contain volcanic ash. Consequently, it could be inferred that the projected paleolatitude for the Keilberg cap dolostone may be lower than the constraint inferred from the paleomagnetic data presented. Nevertheless, this assumption faces a challenge when considering the Marinoan Nantuo Formation situated in South China. This formation, which also harbors volcanic ash, is associated with a paleolatitude of 33°N as determined by highquality paleomagnetic data (Zhang et al., 2013; Q = 7, R = 6). Collectively, these findings propose that the bias toward low-latitude regions in ash deposition on a Snowball Earth may have been influenced by additional factors, possibly including the interplay of ocean currents within

the well-mixed subglacial ocean beneath the ice-covered planet.

In this context, if these sedimentological observations are a compelling reason to reject the primary nature of pole  $C_1$ , then other recent reconstructions for the Congo craton at the beginning of the Ediacaran should also be reevaluated. Modern global full-plate reconstructions (Merdith et al., 2021; Li et al., 2023), based on decades of accumulated paleomagnetic data, position the southwestern margin  $\sim 10^{\circ}$  higher than  $C_1$  at 635 Ma (Fig. 12B). In this regard, a 33° paleolatitude constraint remains a conservative estimate. On the other hand, given the uncertainties inherent in Precambrian paleogeographic reconstructions, the constrained position and orientation of the Congo by  $C_1$  appear to align reasonably well with these reconstructions, which reinforces the notion of a primary pole.

### **5.5.** Magnetostratigraphy and Time Scale for Cap Carbonate Transgression

The presence of at least three polarity reversals at the base of the Keilberg cap dolostone triggers inquiries about the timeframe of deposition and the pace of sedimentation during the context of marine transgression after the rapid

deglaciation following the Marinoan cryochron (Fig. 13).

Assuming an actualistic time for reversals to occur and the average time of a polarity chron (e.g., Gubbins, 1999), the cap dolostone on the Hoanib shelf would have formed over an extremely long period spanning at least hundreds of thousands of years. Even in a hyperactive geomagnetic field, as has been shown to be the case for the Ediacaran, with possibly over 20 reversals per million years (e.g., Levashova et al., 2021), the cap dolostone within the section studied would have formed in  $1.5 \times 10^5$ yr. This duration agrees with estimates from paleomagnetic investigations of other global cap dolostones (Fig. 13; Trindade et al., 2003; Kilner et al., 2005; Schmidt et al., 2009). However, this period considerably exceeds the 2 k.y. deglaciation time scale projected in the ice sheet-energy balance model proposed by Hyde et al. (2000). Additional qualitative indicators, such as the absence of pebble lags or indications of alterations to the original glacial sediments, further suggest a notably swift rise in sea levels during the Cryogenian deglaciation. In the case of cap carbonates, their prompt deposition becomes crucial for preventing dilution by debris influx (like loess), given the prevailing global postglacial conditions (Hoffman et al., 2017). Opting

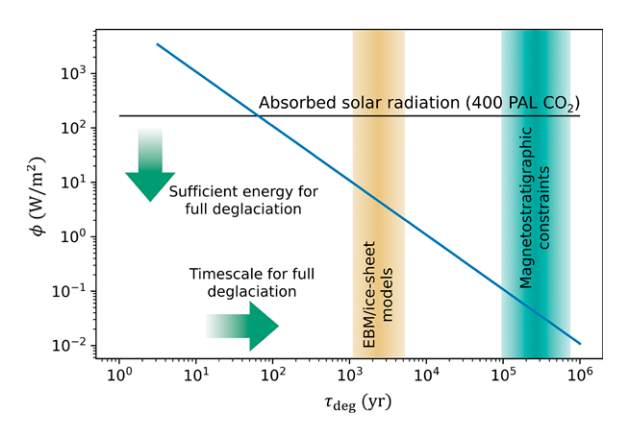


Figure 14. Simplified model for the time scale required for the full deglaciation of a Snowball Earth. Solar radiation absorbed in the post–Snowball Earth hothouse provides sufficient energy for rapid deglaciation, which contradicts estimates derived from magnetostratigraphic constraints. Note the logarithmic scale on both axes, as the required energy flux scales hyperbolically with the reduction in full degla-

ciation time. The blue line represents the time-energy solutions according to Equation 2.

for the prolonged depositional time scale, the sedimentation rate for the Hoanib section, calculated using our paleomagnetic data, would be  $\sim 0.009$  cm/yr. This rate contrasts sharply with rates estimated at 2 cm/yr based on deglaciation models and sedimentological observations (Hoffman, 2011).

The consistency in magnetostratigraphic estimates for the time scale of cap dolostone formation, i.e., TST, both among previous studies (Trindade et al., 2003, 105-106 yr; Kilner et al., 2005, 105-106 yr; Schmidt et al., 2009, 105 yr) and between them and this work (105 yr), suggests a slow deglaciation process (Fig. 13). However, climatic physics imposes constraints that make it challenging to accept such a straightforward conclusion. For instance, assuming that Snowball Earth ice sheets were  $\sim$ 3000 m thick in their central areas, a meltdown occurring over 2000 years would imply an average rate of surface lowering of 1.5 m per year. Comparatively, recent observations show that glacial surfaces in the European Alps and British Columbia (SW Canada) have been decreasing at a rate of 1.6 m/yr (Vincent et al., 2017). Notably, this rate is likely conservative, because most ice sheets during the Snowball Earth period were situated at lower latitudes and therefore received stronger solar irradiance than modern mid-latitude glaciers, such as those in the Alps or Canada. Conversely, Alpine areas have a lower albedo due to the discontinuous nature of glaciers.

One may question whether there is sufficient energy to globally melt ice sheets over a period of 2000 years. According to the principle of conservation of energy, the globally averaged and time-averaged net flux of moist static energy per unit area from Earth's surface, represented as  $\varnothing$ , is defined as:

$$\varnothing = -\Omega_E^{-1} \frac{\partial W}{\partial t}, \tag{1}$$

where  $\Omega_E$  represents Earth's surface area, W represents the combined internal and external energies, and t denotes time (Wallace and Hobbs, 1977). Assuming a simplified model with an average ice thickness of 2 km over all continents and 0.6 km over the ocean, and a ratio of 7:3 for ocean-to-continent surface area, latent heat, and ice density ( $L_{\rm ice}$ ,  $\rho_{\rm ice}$ ), the problem can be reduced to:

$$\phi = ((6 \times 10^2 \times 0.7 + 2 \times 10^3 \times 0.3) \times L_{\text{ice}} \times \rho_{\text{ice}}) / \tau_{\text{deg}},$$
 (2)

where  $au_{\mathrm{deg}}$  is the time required for full deglaciation. For a complete deglaciation occurring over 2000 years, the necessary total energy input ranges between 5 W/m2 and 6 W/m2. While this may seem substantial, it pales in comparison to the  $\sim 167 \text{ W/m}^2$  of solar energy absorbed during the Cryogenian period, assuming a 7% reduction in solar luminosity relative to the present, a CO2 concentration of 400 present atmospheric level, and an average planetary albedo of 0.4 during deglaciation (Le Hir et al., 2009). Thus, there was ample energy available in the post-Snowball Earth hothouse conditions to facilitate rapid deglaciation (Fig. 14). It is important to note that this is a simplified illustrative example and does not consider many important factors, such as the heterogeneity in the distribution of ice caps and the energy losses due to various processes (e.g., heat dissipation). Nonetheless, it serves as a conservative estimate of the speed of deglaciation, as the process scales with positive feedback due to the reduction in albedo during the meltdown (Wu et al., 2021). So, it is physically unlikely that Snowball deglaciation, once started, would have persisted longer than a few thousand years.

Notwithstanding the disparity, suggestions for reconciling between fast deglaciation with magnetostratigraphic constraints were provided by Hoffman et al. (2017), who considered a longer

sea-level rise after deglaciation and anomalous fast geomagnetic reversals.

Ocean warming and thermal expansion, together with glacio-isostatic adjustment modeling (Yang et al., 2017; Creveling and Mitrovica, 2014), indicate that the time scale of marine transgression, under which cap dolostones are formed, can be up to 20 or 30 times longer than the deglaciation time scale of  $\sim$ 2 k.y. (Hoffman et al., 2017). Yet, this time scale is still too rapid to explain the estimates derived from the Keilberg magnetostratigraphy by a factor of five or more, much like for the paleomagnetic estimates in other cap dolostones, as previously noted.

Therefore, the constraints imposed by such models, along with sedimentological-geochemical observations, challenge the estimates based on paleomagnetic data. Hoffman et al. (2017), based on recent propositions of a young inner core (e.g., Bono et al., 2019), argue that should the solid inner core be small or nonexistent, the time scale for a 635 Ma geomagnetic reversal could be substantially shorter than that of more recent reversals, assuming that the reversal time scale is determined by a diffusive process within the solid phase. If so, the estimates of the depositional time of cap dolostones based on magnetostratigraphy could be reduced. While such discussion remains speculative, the observed stratigraphically compressed reversals are likely to be attributed to a magnetic phenomenon (unknown mechanism of remanence acquisition or anomalies in the field) rather than a climatic or sedimentological one. If such a phenomenon proves to be of a global nature, such as extremely rapid reversals, the widespread occurrence of such behavior in Marinoan cap dolostones could be one more argument for their precise temporal correlation (Fig. 13).

#### 5.6. Causes of Remagnetization

The pole derived from the  $C_2$  component pole (CSF11) aligns with the APWP of Gondwana, particularly in the range of poles associated with ages close to 520 Ma (Fig. 10C). This observation, along with a negative fold test, strongly hints at a late-stage remagnetization process. As discussed earlier, the minerals carrying this component consist of fine magnetite falling within the SD grain-size range. Various observations indicate an association between these magnetite particles and the presence of clays and micas within these rocks:

(1) The variation in  $\chi_{hf}$  ( $\geq$ 700 mT) along the stratigraphy, which primarily reflects the concentration of paramagnetic minerals (such as micas and clays) in the samples, roughly follows the changes in NRM intensity.

(2) XRD analyses highlight that samples containing the  $C_2$  component exhibit higher terrigenous mineral content, notably micas and clays such as illite.

(3) Backscattered electron (BSE) images reveal a noticeable textural correlation between magnetite and micas/clays.

Collectively, these findings direct the interpretation toward a remagnetization mechanism that involves the transformation of iron-rich smectite into iron-poor illite (e.g., Katz et al., 2000; Jackson et al., 1988; Tohver et al., 2008; Hirt et al., 1993). Experimental observations regarding the authigenesis of magnetic minerals within clayey carbonates under the influence of temperature are also well-established (Moreau et al., 2005).

The process that converts smectites into illites involves a chemical-mineral reaction that occurs during diagenesis as sedimentary layers undergo progressive burial. Within this transformation, expansive smectites transition into non-expansive illites (Hower et al., 1976; Boles and Franks, 1979). This reaction is particularly prominent within a temperature range of 70–150 °C. The conversion process necessitates a supply of K + ions (Weaver, 1958). These ions can originate from various sources, and in our context, they are likely derived from the decomposition of potassium feldspar and detrital micas at temperatures ranging between 40° C to 80 °C. Importantly, this conversion can occur without the need for external fluids. Trioctahedral smectites containing divalent cations like Fe<sup>2+</sup> and Mg2+ undergo full conversion only at temperatures surpassing 100 °C. This limitation arises due to the chemical constraints of trioctahedral aluminous clays, which hinder the development of expansive structures necessary for effective potassium ion fixation at temperatures below 100 °C. As diagenesis advances and metamorphism commences, the transformation of illite into aluminous micas takes place at temperatures exceeding 150 °C (Boles and Franks, 1979).

The alteration process of smectite into illite leads to the liberation of Fe<sup>3+</sup> cations, which have the potential to engage in reactions giving rise to a diverse array of minerals, one of which is magnetite. In our interpretation, this process gave rise to the fine magnetite that carries remanence in  $C_2$ -bearing rocks, since such remanent magnetization is observed within the clay-rich portion of the Maieberg succession.

Another plausible scenario could involve the generation of authigenic magnetite through the percolation of external fluids, given the nearby orogenetic setting that could facilitate such a process. However, studies employing isotopic proxies suggest that meteoric diagenesis or fluid-mediated alteration was not a prevalent phenomenon in Otavi platform carbonates.

Kaufman et al. (1991) arrived at this conclusion by comparing  $\delta^{13}C$  values in microspar (a less altered phase) with those of the whole rock, which showed a nearly 1:1 ratio. Similarly, Halverson et al. (2002) reached the same conclusion in the Ombaatjie Formation (pre-Ghaub) after examining  $\delta^{18}O$  and  $\delta^{13}C$  values along with the Mn/Sr ratio. Moreover, there is a lack of textural evidence in our samples to support the notion of magnetic mineral generation through fluid percolation. Based on these comprehensive investigations and observations, it appears that there is not a direct association between meteoric diagenesis or the influx of orogenic fluids and the remagnetization process.

Consequently, we posit that the main remagnetization mechanism impacting the Maieberg carbonates was the thermochemical process. This early diagenetic transformation, occurring at low temperatures and influenced by depth and Kaoko anchimetamorphism, probably keeps the magnetic system reset until the Cambrian due to the low relaxation time of magnetite under formation at low-temperature conditions (Pullaiah et al., 1975). The timing of the Kaoko orogen exhumation and cooling phase (ca. 530–525 Ma, Foster et al., 2009) fits well with the position of the  $C_2$  pole on the Gondwana APWP, when the magnetic system should have been locked.

Taking these factors into account, the remagnetization model proposed for the Maieberg carbonates develops as follows: (1) deposition of iron-rich smectites during the carbonate sedimentation phase, (2) formation of authigenic magnetite through the Fe released during the smectite/illite transformation in early diagenesis, (3) sustained openness of the magnetic system during the late diagenesis and anchimetamorphic phase, (4) closure of the magnetic system and acquisition of remanence during the exhumation and tectonic uplift phase (525–520 Ma), and (5) subsequent preservation of remanence followed by erosion.

The CSF11 pole derived for the Maieberg carbonates closely aligns in both spatial and temporal aspects with poles obtained from other remagnetized Neoproterozoic carbonates within West Gondwana. This similarity prompts inquiries regarding the possible common origin of these remagnetization processes. However, exploring these aspects is beyond the scope of our present study.

#### 6. CONCLUSION

In this study, our focus was on investigating the paleomagnetism of the basal Maieberg Formation cap carbonates along the Hoanib Shelf in Namibia. Our objectives included describing the magnetic properties of these rocks, determining the paleolatitude at the time of their formation, and establishing connections with similar cap carbonate and glaciogenic units worldwide. Ultimately, we aimed to glean insights into the SBE postglacial dynamics.

We obtained two distinct components. The first, named  $C_1$ , is carried by PSD magnetite and is interpreted as detrital. The second, referred to as  $C_2$ , which is carried by SD-PSD magnetite, is interpreted as authigenic in origin. While the possibility of a syn-folding remagnetization during the Kaoko metamorphism at ca. 580-570 Ma for the  $C_1$  component cannot be dismissed, we lean toward interpreting it as a primary magnetization. This preference arises from the rock magnetic signatures, simpler remanence acquisition mechanism, the existence of reversals, and its consistency with paleogeographic models. On the other hand,  $C_2$  was confirmed as a remagnetization through a fold test and its pole position within the Early Cambrian section of the West Gondwana APWP.

The sedimentation paleolatitude derived from  $C_1$  is  $33.3^{\circ} \pm 3.2^{\circ}$  at ca. 635 Ma. By extension, this provides the first quantitative paleolatitude approximation to the important Marinoan Ghaub glaciogenic deposits. This paleolatitude, when considered alongside the existing compilation of paleomagnetic data from glaciogenic units and cap carbonates, lends further support to the SBE theory's proposition of widespread glacial processes during the Marinoan times, spanning a wide range of latitudes.

As indicated in previous paleogeographic models, the calculated paleolatitude of the Keilberg member using the  $C_1$  component appears to be unusually elevated when considering its thickness and the paleogeographical distribution of cap dolostones during the Cryogenian period. This suggests that instead of relying solely on the temperature (latitude) dependence in carbonate oversaturation, other factors must have contributed to the overall thickness of the Maieberg flooding carbonate sequence. We propose that the local impact of alkalinity input together with a large accommodation space, formed through local tectonic subsidence during an extended glacial period with exceptionally low sedimentation rates, must have played an important role.

Like other Marinoan cap dolostones, the Keilberg Member exhibits more than one geomagnetic field reversal at its base. Assuming the duration of a modern geomagnetic polarity and reversal, this implies a much longer time scale for marine transgression than climate physics, deglaciation models, and sedimentological-geochemical observations have constrained. Whole-ocean warming, thermal expansion, and glacio-isostatic adjustments suggest that marine transgressions, linked to cap dolostone

deposition, can last significantly longer than the relatively rapid deglaciation events. Still, magnetostratigraphic estimates for cap dolostone deposition have consistently appeared too rapid, by a factor of five or more. Together, such arguments challenge the interpretation of the time scale based on paleomagnetic data, and we interpret that the stratigraphically compressed expression of these reversals is probably a magnetic phenomenon yet to be understood rather than a climatic or sedimentological one.

The pole from the  $C_2$  component is very close to the West Gondwana Cambrian remagnetization poles (ca. 520 Ma) observed in other carbonate units from São Francisco and the Amazonian cratons. This correlation now extends to the Congo craton, which implies an event of even greater scale. Based on the dataset presented in our investigation, we propose that the physical process responsible for the acquisition of remanence in  $C_2$ -carrying rocks is associated with the transformation of iron-rich smectites into iron-poor illites during burial diagenesis. As a result, fine authigenic magnetite formed as a byproduct of this reaction. With the advancement of diagenesis and the prolonged low-grade metamorphism, the magnetic system must have remained open until it was eventually locked due to uplift and cooling. This cooling event is possibly linked to the period of exhumation and tectonic uplift in the Kaoko orogen. This interpretation is supported by the position of the  $C_2$ pole on the APWP of West Gondwana, but other explanations are possible.

#### ACKNOWLEDGMENTS

We thank FAPESP (Brazil) for providing financial support for this research, associated with grants 03/11143-5 and 16/06114-6. The opinions, hypotheses, conclusions, or recommendations expressed in this material are solely the responsibility of the authors and do not necessarily represent the views of FAPESP. T. Pescarini is supported by a research fellowship from FAPESP (20/03347-5). P.F. Hoffman acknowledges financial support from U.S. National Science Foundation grant EAR-99-05495 and Harvard University. We are grateful for the comments and suggestions of Augusto Rapalini, Massimo Mattei, and an anonymous reviewer who helped to improve this work, and the editorial work of Mihai Ducea.

#### REFERENCES CITED

- Abrajevitch, A., and Van der Voo, R., 2010, Incompatible Ediacaran paleomagnetic directions suggest an equatorial geomagnetic dipole hypothesis: Earth and Planetary Science Letters, v. 293, p. 164–170, https://doi.org/10
- Allen, P.A., and Hoffman, P.F., 2005, Extreme winds and waves in the aftermath of a Neoproterozoic glaciation: Nature, v. 433, p. 123–127, https://doi.org/10.1038/nature03176.
- Antonio, P.Y.J., Trindade, R.I.F., Giacomini, B., Brandt, D., and Tohver, E., 2021, New high-quality paleomagnetic data from Borborema Province (NE Brazil): Refinement of the APW path of Gondwana in the Early Cam-

- brian: Precambrian Research, v. 360, https://doi.org/10.1016/j.precamres.2021.106243.
- Basei, M.A.S., Frimmel, H.E., Campos Neto, M.C., Araújo, C.E.G., Castro, N.A., and Passarelli, C.R., 2018, The tectonic history of the southern Adamastor ocean based on a correlation of the Kaokoan Dom Feliciano belts, in Siegesmund, S., Basei, M., Oyhantçabal, P., and Oriolo, S., eds., Geology of Southwest Gondwana: Cham, Switzerland, Springer, Regional Geology Reviews, p. 63–85, https://doi.org/10.1007/978-3-319-68920-3
- Bold, U., Smith, E.F., Rooney, A.D., Bowring, S.A., Buchwaldt, R., Dudás, F.Ö., Ramezani, J., Crowley, J.L., Schrag, D.P., and Macdonald, F.A., 2016, Neoproterozoic stratigraphy of the Zavkhan terrane of Mongolia: The backbone for Cryogenian and early Ediacaran chemostratigraphic records: American Journal of Science, v. 316, p. 1–63, https://doi.org/10.2475/01.2016.01.
- Boles, J.R., and Franks, S.G., 1979, Clay diagenesis in Wilcox sandstones of Southwest Texas; implications of smectite diagenesis on sandstone cementation: Journal of Sedimentary Research, v. 49, no. 1, p. 55–70, https://doi.org/10.1306/212F76BC-2B24-11D7-8648000102C1865D.
- Bono, R.K., Tarduno, J.A., Nimmo, F., and Cottrell, R.D., 2019, Young inner core inferred from Ediacaran ultralow geomagnetic field intensity: Nature Geoscience, v. 12, no. 2, p. 143–147, https://doi.org/10.1038 /s41561-018-0288-0.
- Boyden, J.A., Muller, D., Gurnis, M., Torsvik, T.H., Clark, J.A., Turner, M., Ivey-Law, H., Watson, R.J., and Cannon, J., 2011 Next-generation plate-tectonic reconstructions using GPlates, in Keller, G.R., and Baru, C., eds., Geoinformatic: Cyberinfrastructure for Solid Earth Sciences: Cambridge, UK, Cambridge University Press, p. 95–114, https://doi.org/10.1017 /CBO9780511976308.008.
- Briden, J.C., 1968, Palaeomagnetism of the Ntonya Ring Structure, Malawi: Journal of Geophysical Research, v. 73, p. 725–733, https://doi.org/10.1029 /JB073i002p00725.
- Budyko, M.I., 1969, The effect of solar radiation variations on the climate of the Earth: Tellus, v. 21, no. 5, p. 611– 619, https://doi.org/10.3402/tellusa.v21i5.10109.
- Butler, R.F., 1992, Paleomagnetism: Magnetic Domains to Geological Terranes: Oxford, UK, Blackwell Scientific Publications.
- Carvallo, C., Muxworthy, A.R., and Dunlop, D., 2006, First-order reversal curve (FORC) diagrams of magnetic mixtures: Micromagnetic models and measurements: Physics of the Earth and Planetary Interiors, v. 154, p. 308–322, https://doi.org/10.1016/j.pepi.2005.06.017.
- Coward, M.P., 1981, The junction between Pan African Mobile belts in Namibia: Its structural history: Tectonophysics, v. 76, p. 59–73, https://doi.org/10.1016 /0040-1951(81)90253-5.
- Creveling, J.R., and Mitrovica, J.X., 2014, The sea-level fingerprint of a Snowball Earth deglaciation: Earth and Planetary Science Letters, v. 399, p. 74–85, https://doi.org/10.1016/j.epsl.2014.04.029.
- Cukjati, A., Franceschinis, P.R., Arrouy, M.J., Gómez Peral, L.E., Poiré, D.G., Trindade, R.I.F., and Rapalini, A.E., 2023, The Ediacaran apparent polar wander path of the Río de la Plata craton revisited: Paleogeographic implications: Precambrian Research, v. 397, https://doi.org/ /10.1016/j.precamres.2023.107205.
- D'Agrella-Filho, M.S., and Pacca, I., 1988, Paleomagnetism of the Itajaí and Bom Jardim Group from Southern Brazil: Geophysical Journal International, v. 93, p. 365–376, https://doi.org/10.1111/j.1365-246X.1988.tb02008.x.
- D'Agrella-Filho, M.S., Pacca, I.G., and Sato, K., 1986, Paleomagnetism of metamorphic rocks from the Piquete region—Ribeira Valley, Southeastern Brazil: Revista Brasileira de Geofísica, v. 4, p. 79–84, https://doi.org/10.22564/rbgf.v4i2.1039.
- D'Agrella-Filho, M.S., Pacca, I.I.G., Trindade, R.I.F., Teixeira, W., Raposo, M.I.B., and Onstott, T.C., 2004, Paleomagnetism and <sup>40</sup>Ar<sup>39</sup>Ar ages of mafic dikes from Salvador (Brazil): New constraints on the São Francisco craton APW path between 1080 and 1010 Ma: Precambrian Research, v. 132, p. 55–77, https://doi.org/10.1016/j.precamres.2004.02.003.

- Day, R., Fuller, M., and Schimidt, V.A., 1977, Hysteresis properties of titanomagnetites—Grain size and compositional dependence: Physics of the Earth and Planetary Interiors, v. 13, p. 260–267, https://doi.org/10.1016 //0031-9201(77)90108-X.
- Denyszyn, S.W., Davis, D.W., and Halls, H.C., 2009, Paleomagnetism and U-Pb geochronology of the Clarence Head dykes, Arctic Canada: Orthogonal emplacement of mafic dykes in a large igneous province: Canadian Journal of Earth Sciences, v. 46, no. 3, p. 155–167, https://doi.org/10.1139/E09-011.
- Dunlop, D., 2002a, Theory and application of the Day plot (M<sub>rs</sub>/M<sub>r</sub> versus H<sub>c</sub>/H<sub>c</sub>): 1. Theoretical curves and tests using titanomagnetite data: Journal of Geophysical Research: Solid Earth, v. 107, no. B3, https://doi.org/10.1029/2001JB000486.
- Dunlop, D., 2002b, Theory and application of the Day plot (Mrs/Ms versus Hcr/Hc): 2. Application to data for rocks, sediments, and soils: Journal of Geophysical Research: Solid Earth, v. 107, no. B3, p. EPM 5-1-EPM 5-15, https://doi.org/10.1029/2001JB000487.
- Dunlop, D.J., and Özdemir, Ö., 1997, Rock Magnetism: Fundamentals and Frontiers: New York, Cambridge University Press, https://doi.org/10.1017/CBO 9780511612794.
- Egli, R., 2003, Analysis of the field dependence of remanent magnetization curves: Journal of Geophysical Research: Solid Earth, v. 108, no. B2, https://doi.org/10 1029/20021B002023.
- Egli, R., 2004, Characterization of individual rock magnetic components by analysis of remanence curves: Unmixing natural sediments: Studia Geophysica et Geodaetica, v. 48, p. 391–446, https://doi.org/10.1023/B:SGEG .0000020839.45304.6d.
- Evans, D.A.D., 2000, Stratigraphic, geochronological and paleomagnetic constraints upon the Neoproterozoic climatic paradox: American Journal of Science, v. 300, p. 347–433, https://doi.org/10.2475/ajs.300.5.347.
- Evans, D.A.D., and Raub, T.D., 2011, Neoproterozoic glacial palaeolatitudes: A global update, in Arnaud, E., Halverson, G.P., and Shields-Zhou, G., eds., The Geological Record of Neoproterozoic Glaciations: Geological Society, London, Memoir 36, p. 93–112, https://doi.org //10.1144/M36.7.
- Evans, D.A.D., et al., 2021, An expanding list of reliable paleomagnetic poles for Precambrian tectonic reconstructions, in Pesonen, L.J., Salminen, J., Elming, S.Å., Evans, D.A.D., and Veikkolainen, T., eds., Ancient Supercontinents and the Paleogeography of Earth: Amsterdam, Elsevier, p. 605–639, https://doi.org/10 .1016/B978-0-12-818533-9.00007-2.
- Fisher, R.A., 1953, Dispersion on a sphere: Proceedings of the Royal Society A: Mathematical, Physical and Engineering Sciences, v. 217, p. 295–305, https://doi.org/10 .1098/rspa.1953.0064.
- Foster, D.A., Goscombe, B.D., and Gray, D.R., 2009, Rapid exhumation of deep crust in an obliquely convergent orogen: The Kaoko Belt of the Damara Orogen: Tectonics, v. 28, https://doi.org/10.1029/2008TC002317.
- Franceschinis, P.R., Rapalini, A.E., Escayola, M.P., and Rodríguez Piceda, C., 2020, Paleogeographic and tectonic evolution of the Pampia Terrane in the Cambrian: New paleomagnetic constraints: Tectonophysics, v. 779, https://doi.org/10.1016/j.tecto.2020.228386.
- Gevers, T.W., 1931, An ancient tillite in South-West Africa: Transactions of the Geological Society of South Africa, v. 34, p. 1–17.
- Geyman, E.C., et al., 2022, The origin of carbonate mud and implications for global climate: Proceedings of the National Academy of Sciences of the United States of America, v. 119, no. 43, https://doi.org/10.1073/pnas .2210617119.
- Goodman, J.C., and Pierrehumbert, R.T., 2003, Glacial flow of floating marine ice in "Snowball Earth": Journal of Geophysical Research: Oceans, v. 108, no. C10, https://doi.org/10.1029/2002JC001471.
- Goodman, J.C., and Strom, D.C., 2013, Feedbacks in a coupled ice-atmosphere-dust model of the glacial Neoproterozoic "Mudball Earth": Journal of Geophysical Research, v. 118, p. 11,546–11,557, https://doi.org/10 .1002/jgrd.50849.

- Goscombe, B.D, Gray, D.R, Armstrong, R.A, Foster, D.A., and Vogl, J., 2005, Event geochronology of the Pan-African Kaoko Belt, Namibia: Precambrian Research, v. 140, p. 103.e1–103.e41, https://doi.org/10.1016/j .precamres.2005.07.003.
- Goscombe, B.D., Foster, D.A., Gray, D.R., and Wade, B., 2018, The evolution of the Damara orogenic system: A record of West Gondwana assembly and crustal response, *in* Siegesmund, S., Basei, M.A.S., Oyhantçabal, P., and Oriolo, S., eds., Geology of Southwest Gondwana: Cham, Switzerland, Springer, Regional Geology Reviews, p. 303–352, https://doi.org/10.1007/978-3-319-68920-3\_12.
- Graham, J.W., 1949, The stability and significance of magnetism in sedimentary rocks: Journal of Geophysical Research, v. 54, p. 131–167, https://doi.org/10.1029/JZ054i002p00131.
- Gray, D.R., Foster, D.A., Goscombe, B.D., Passchier, C.W., and Trouw, R.A.J., 2006, 40Ar/39Ar thermochronology of the Pan-African Damara orogen, Namibia, with implications for tecto-nonthermal and geodynamic evolution: Precambrian Research, v. 150, p. 49–72, https://doi.org/10.1016/j.precamres.2006.07.003.
- Gray, D.R., Foster, D.A., Meert, J.G., Goscombe, B.D., Armstrong, R.A., Trouw, R.A.J., and Passchier, C.W., 2008, A Damara orogen perspective on the assembly of southwestern Gondwana: Geology, v. 294, p. 257–278, https://doi.org/10.1144/SP294.14.
- Gubbins, D., 1999, The distinction between geomagnetic excursions and reversals: Geophysical Journal International, v. 137, p. F1–F4, https://doi.org/10.1046/j .1365-246x.1999.00810.x.
- Halverson, G.P., Hoffman, P.F., Schrag, D.P., and Kaufman, A.J., 2002, A major perturbation of the carbon cycle before the Ghaub glaciation (Neoproterozoic) in Namibia: Prelude to snowball Earth?: Geochemistry, Geophysics, Geosystems, v. 3, p. 1–24, https://doi.org/10.1029 /2001GC000244.
- Halverson, G.P., Hoffman, P.F., Schrag, D.P., Maloof, A.C., and Rice, A.H.N., 2005, Toward a Neoproterozoic composite carbon-isotope record: Geological Society of America Bulletin, v. 117, p. 1181–1207, https://doi .org/10.1130/B25630.1.
- Heslop, D., and Roberts, A.P., 2018, Revisiting the paleomagnetic reversal test: A Bayesian hypothesis testing framework for a common mean direction: Journal of Geophysical Research: Solid Earth, v. 123, p. 7225–7236, https://doi.org/10.1029/2018JB016081.
- Heslop, D., Roberts, A.P., Oda, H., Zhao, X., Harrison, R.J., Muxworthy, A.R., Hu, P.X., and Sato, T., 2020, An automatic model selection-based machine learning framework to estimate FORC distributions: Journal of Geophysical Research: Solid Earth, v. 125, no. 10, https://doi.org/10.1029/2020JB020418.
- Higgins, J.A., and Schrag, D.P., 2003, Aftermath of a Snowball Earth: Geochemistry, Geophysics, Geosystems, v. 4, no. 3, https://doi.org/10.1029/2002GC000403.
- Hirt, A.M., Banin, A., and Gehring, A.U., 1993, Thermal generation of ferromagnetic minerals from iron-enriched smectites: Geophysical Journal International, v. 115, p. 1161–1168, https://doi.org/10.1111/j .1365-246X.1993.tb01518.x.
- Hoffman, P.F., 2002, Carbonates bounding glacial deposits: Evidence for Snowball Earth episodes and greenhouse aftermaths in the Neoproterozoic Otavi Group of northern Namibia: Field Excursion Guidebook, International Association of Sedimentologists.
- Hoffman, P.F., 2011, Strange bedfellows: Glacial diamictite and cap carbonate from the Marinoan (635 Ma) glaciation in Namibia: Sedimentology, v. 58, p. 57–119, https://doi.org/10.1111/j.1365-3091.2010.01206.x.
- Hoffman, P.F., 2021, On the kinematics and timing of Rodinia breakup: A possible rift-transform junction of Cryogenian age at the southwest cape of Congo craton (northwest Namibia): South African Journal of Geology, v. 124, no. 2, p. 401–420, https://doi.org/10.25131/sajg.124.0038.
- Hoffman, P.F., and Halverson, G.P., 2008, Otavi Group of the western Northern platform, the eastern Kaoko Zone and the western Northern Margin Zone, in Miller, R.M., ed., The Geology of Namibia, Volume 2: Windhoek, Geological Survey of Namibia, p. 13.69–13.136.

- Hoffman, P.F., and Li, Z.X., 2009, A palaeogeographic context for Neoproterozoic glaciation: Palaeogeography, Palaeoclimatology, Palaeoecology, v. 277, p. 158–172, https://doi.org/10.1016/j.palaeo.2009.03.013.
- Hoffman, P.F., and Macdonald, F.A., 2010, Sheet-crack cements and early regression in Marinoan (635 Ma) cap dolostones: Regional benchmarks of vanishing ice-sheets?: Earth and Planetary Science Letters, v. 300, p. 374–384, https://doi.org/10.1016/j.epsl.2010.10.027.
- Hoffman, P.F., and Schrag, D.P., 2002, The snowball Earth hypothesis: Testing the limits of global change: Terra Nova, v. 14, p. 129–155, https://doi.org/10.1046/j.1365-3121.2002.00408.x.
- Hoffman, P.F., Hawkins, D.P., Isachsen, C.E., and Bowring, S.A., 1996, Precise U-Pb zircon ages for early Damaran magmatism in the Summas Mountains and Welwitschia Inlier, northern Damara Belt, Namibia: Communications of the Geological Survey of Namibia, v. 11, p. 47–52.
- Hoffman, P.F., Kaufman, A.J., Halverson, G.P., and Schrag, D.P., 1998, A Neoproterozoic snowball Earth: Science, v. 281, p. 1342–1346, https://doi.org/10.1126/science .281.5381.1342.
- Hoffman, P.F., Halverson, G.P., Domack, E.W., Husson, J.M., Higgins, J.A., and Schrag, D.P., 2007, Are basal Ediacaran (635 Ma) postglacial "cap dolostones" diachronous?: Earth and Planetary Science Letters, v. 258, no. 1–2, p. 114–131, https://doi.org/10.1016/j.epsl.2007 .03.032.
- Hoffman, P.F., et al., 2017, Snowball Earth climate dynamics and Cryogenian geology-geobiology: Science Advances, v. 3, no. 11, https://doi.org/10.1126/sciadv.1600983.
- Hoffman, P.F., et al., 2021, Snowballs in Africa: Sectioning a long-lived Neoproterozoic carbonate platform and its bathyal foreslope (NW Namibia): Earth-Science Reviews, v. 219, https://doi.org/10.1016/j.earscirev.2021 .103616.
- Hoffmann, K.-H., Condon, D.J., Bowring, S.A., and Crowley, J.L., 2004, A U-Pb zircon date from the Neoproterozoic Ghaub Formation, Namíbia: Constraints on Marinoan glaciation: Geology, v. 32, p. 817–820, https://doi.org /10.1130/G20519.1.
- Hower, J., Eslinger, E.V., Hower, M.E., and Perry, E.A., 1976, Mechanism of burial metamorphism of argillaceous sediments: 1, Mineralogical and chemical evidence: Geological Society of America Bulletin, v. 87, p. 725–737, https://doi.org/10.1130 /0016-7606(1976)87<725:MOBMOA>2.0.CO;2.
- Hyde, W.T., Crowley, T.J., Baum, S.K., and Peltier, W.R., 2000, Neoproterozoic 'Snowball Earth' simulations with a coupled climate/ice-sheet model: Nature, v. 405, p. 425–429, https://doi.org/10.1038/35013005.
- Jackson, M., 1990, Diagenetic sources of stable remanence in remagnetized Paleozoic cratonic carbonates: A rock magnetic study: Journal of Geophysical Research: Solid Earth, v. 95, p. 2753–2761, https://doi.org/10 .1029/JB095iB03p02753.
- Jackson, M., and Swanson-Hysell, N.L., 2012, Rock magnetism of remagnetized carbonate rocks: Another look, in Elmore, R.D., Muxworthy, A.R., Aldana, M.M., and Mena, M., eds., Remagnetization and Chemical Alteration of Sedimentary Rocks: Geological Society, London, Special Publication 371, p. 229–251, https://doi.org/10.1144/SP371.3.
- Jackson, M., McCabe, C., Ballard, M.M., and Van der Voo, R., 1988, Magnetite authigenesis and diagenetic paleotemperatures across the northern Appalachian basin: Geology, v. 16, p. 592–595, https://doi.org/10.1130 //0091-7613(1988)016<0592:MAADPA>2.3.CO;2.
- Jiang, L.Q., Feely, R.A., Carter, B.R., Greeley, D.J., Gledhill, D.K., and Arzayus, K.M., 2015, Climatological distribution of aragonite saturation state in the global oceans: Global Biogeochemical Cycles, v. 29, p. 1656–1673, https://doi.org/10.1002/2015GB005198.
- Katz, B., Elmore, D.R., Cogoini, M., Engel, M.H., and Ferry, S., 2000, Associations between burial diagenesis of smectite, chemical remagnetization, and magnetite authigenesis in the Vocontian trough, SE France: Journal of Geophysical Research: Solid Earth, v. 105, p. 851– 868, https://doi.org/10.1029/1999JB900309.
- Kaufman, A.J., Hayes, J.M., Knoll, A.H., and Germs, G.J.B., 1991, Isotopic compositions of carbonates and organic

- carbon from upper Proterozoic successions in Namibia: Stratigraphic variation and the effects of diagenesis and metamorphism: Precambrian Research, v. 49, p. 301–327, https://doi.org/10.1016/0301-9268(91)90039-D.
- Kempf, O., Kellerhals, P., Lowrie, W., and Matter, A., 2000, Paleomagnetic directions in Late Precambrian glaciomarine sediments of the Mirbat Sandstone Formation, Oman: Earth and Planetary Science Letters, v. 175, p. 181–190, https://doi.org/10.1016/S0012-821X (99)00307-6.
- Kilner, B., MacNiocaill, C., and Brasier, M., 2005, Low-latitude glaciation in the Neoproterozoic of Oman: Geology, v. 33, p. 413–416, https://doi.org/10.1130/G21227.1.
- Kirschvink, J.L., 1980, The least-squares line and plane and the analysis of paleomagnetic data: Geophysical Journal International, v. 62, no. 3, p. 699–718, https://doi .org/10.1111/j.1365-246X.1980.tb02601.x.
- Kirschvink, J.L., 1992, Late Proterozoic low-latitude global glaciation: The Snowball Earth, in Schopf, J.W., and Klein, C., eds., The Proterozoic Biosphere: A Multidisciplinary Study: New York, Cambridge University Press.
- Kirschvink, J.L., Higgins, M.D., Evans, D.A.D, Condon, D.J., Raub, T.D., Bowring, S.A., Nowlan, G.S., Macdonald, F.A., and Farley, K.A., 2005, Ediacaran rapid true polar wander: Constraints on a possible driving mechanism from the paleomagnetism and geochronology of the Sept-Îles Intrusive Suite, Quebéc, Canada: Eos (Transactions, American Geophysical Union), v. 86, Joint Assembly Supplement, abstract GP21A-05.
- Kodama, K.P., 2021, Combined magnetostratigraphy from three localities of the Rainstorm Member of the Johnnie Formation in California and Nevada, United States calibrated by cyclostratigraphy: A 13 R/Ma reversal frequency for the Ediacaran: Frontiers of Earth Science, v. 9, https://doi.org/10.3389/feart.2021.764714.
- Le Hir, G., Ramstein, G., Donnadieu, Y., and Goddéris, Y., 2008, Scenario for the evolution of atmospheric pCO<sub>2</sub> during a snowball Earth: Geology, v. 36, p. 47–50, https://doi.org/10.1130/G24124A.1.
- Le Hir, G., Donnadieu, Y., Goddéris, Y., Pierrehumbert, R.T., Halverson, G.P., Macouin, M., Nédélec, A., and Ramstein, G., 2009, The snowball Earth aftermath: Exploring the limits of continental weathering processes: Earth and Planetary Science Letters, v. 277, p. 453–463, https://doi.org/10.1016/j.epsl.2008.11.010.
- Levashova, N.M., Golovanova, I.V., Rudko, D.V., Danukalov, K.N., Rudko, S.V., Yu, S.R., and Meert, J.G., 2021, Late Ediacaran magnetic field hyperactivity: Quantifying the reversal frequency in the Zigan Formation, Southern Urals, Russia: Gondwana Research, v. 94, p. 133–142, https://doi.org/10.1016/j.gr.2021.02.018.
- Lloyd, S.J., Biggin, A.J., Halls, H., and Hill, M.J., 2021, First palaeointensity data from the Cryogenian and their potential implications for inner core nucleation age: Geophysical Journal International, v. 226, p. 66–77, https://doi.org/10.1093/gji/ggab090.
- Li, D.W., and Pierrehumbert, R.T., 2011, Sea glacier flow and dust transport on Snowball Earth: Geophysical Research Letters, v. 38, no. 17, https://doi.org/10.1029 /2011GL048991.
- Li, Z.X., 2000, New palaeomagnetic results from the 'cap dolomite' of the Neoproterozoic Walsh Tillite, northwestern Australia: Precambrian Research, v. 100, p. 359–370, https://doi.org/10.1016/S0301-9268 (99)00081-9.
- Li, Z.X., et al., 2008, Assembly, configuration, and break-up history of Rodinia: A synthesis: Precambrian Research, v. 160, p. 179–210, https://doi.org/10.1016/j.precamres 2007.04.021.
- Li, Z.X., Evans, D.A.D., and Halverson, G.P., 2013, Neoproterozoic glaciations in a revised global palaeogeography from the breakup of Rodinia to the assembly of Gondwanaland: Sedimentary Geology, v. 294, p. 219– 232, https://doi.org/10.1016/j.sedgeo.2013.05.016.
- Li, Z.X., Liu, Y., and Ernst, R., 2023, A dynamic 2000–540 Ma Earth history: From cratonic amalgamation to the age of supercontinent cycle: Earth-Science Reviews, v. 238, https://doi.org/10.1016/j.earscirev.2023.104336.
- Maxbauer, D.P., Feinberg, J.M., and Fox, D.L., 2016, MAX UnMix: A web application for unmixing magnetic

- coercivity distributions: Computers & Geosciences, v. 95, p. 140–145, https://doi.org/10.1016/j.cageo.2016.07.009.
- McCausland, P., Van der Voo, R., and Hall, C., 2007, Circum-Iapetus paleogeography of the Precambrian–Cambrian transition with a new paleomagnetic constraint from Laurentia: Precambrian Research, v. 156, p. 125–152, https://doi.org/10.1016/j.precamres.2007.03.004.
- Meert, J.G., and Van der Voo, R., 1996, Paleomagnetic and <sup>40</sup>Ar/<sup>39</sup>Ar study of the Sinyai dolerite, Kenya: Implications for Gondwana assembly: The Journal of Geology, v. 104, p. 131–142, https://doi.org/10.1086/629810.
- Meert, J.G., Van der Voo, R., and Ayub, S., 1995, Paleomagnetic investigation of the Neoproterozoic Gagwe lavas and Mbozi complex, Tanzania and the assembly of Gondwana: Precambrian Research, v. 74, p. 225–244, https://doi.org/10.1016/0301-9268(95)00012-T.
- Meert, J.G., Nédélec, A., Hall, C., Wingate, M.T.D., and Rakotondrazafy, M., 2001, Paleomagnetism, geochronology and tectonic implications of the Cambrian-age Carion granite, Central Madagascar: Tectonophysics, v. 340, p. 1–21, https://doi.org/10.1016/S0040-1951 (01)00163-9.
- Meert, J.G., Nédélec, A., and Hall, C., 2003, The stratoid granites of central Madagascar: Paleomagnetism and further age constraints on neoproterozoic deformation: Precambrian Research, v. 120, p. 101–129, https://doi.org/10.1016/S0301-9268(02)00161-4.
- Meert, J.G., Pivarunas, A.F., Evans, D.A.D., Pisarevsky, S.A., Pesonen, L.J., Li, Z.X., and Salminen, J.M., 2020, The magnificent seven: A proposal for modest revision of the quality index: Tectonophysics, v. 790, https://doi. org/10.1016/j.tecto.2020.228549.
- Merdith, A.S., Williams, S.E., Collins, A.S., Tetley, M.G., Mulder, J.A., Blades, M.L., and Müller, R.D., 2021, Extending full-plate tectonic models into deep time: Linking the Neoproterozoic and the Phanerozoic: Earth-Science Reviews, v. 214, https://doi.org/10.1016 /j.earscirev.2020.103477.
- Miller, R.M., 1983, The Pan-African Damara Orogen of Namibia, in Miller, R.M., ed., Evolution of the Damara Orogen of South West Africa/Namibia: Geological Society of South Africa Special Publication 11, p. 431–515.
- Millero, F.J., 1979, The thermodynamics of the carbonate system in seawater: Geochimica et Cosmochimica Acta, v. 43, p. 1651–1661, https://doi.org/10.1016 /0016-7037(79)90184-4.
- Mitchell, R.N., Kilian, T.M., Raub, T.D., Evans, D.A.D., Bleeker, W., and Maloof, A.C., 2011, Sutton hotspot: Resolving Ediacaran–Cambrian tectonics and true polar wander for Laurentia: American Journal of Science, v. 311, no. 8, p. 651–663, https://doi.org/10.2475/08 .2011.01.
- Moloto-A-Kenguemba, G., Trindade, R.I.F., Monié, P., Nédélec, A., and Siqueira, R., 2008, A late Neoproterozoic paleomagnetic pole for the Congo craton: Tectonic setting, paleomagnetism and geochronology of the Nola dike swarm (Central African Republic): Precambrian Research, v. 164, p. 214–226, https://doi.org/10.1016/j.precamres.2008.05.005.
- Moreau, M.G., Ader, M., and Enkin, R.J., 2005, The magnetization of clay-rich rocks in sedimentary basins: Low-temperature experimental formation of magnetic carriers in natural samples: Earth and Planetary Science Letters, v. 230, p. 193–210, https://doi.org/10.1016/j.epsl.2004.11.013.
- Nairn, A.E.M., Perry, T.A., Ressetar, R., and Rogers, S., 1987, A paleomagnetic study of the Dokhan volcanic formation and younger granites, eastern desert of Egypt: Journal of African Earth Sciences, v. 6, p. 353– 365, https://doi.org/10.1016/0899-5362(87)90078-9.
- Opdyke, B.N., and Wilkinson, B.H., 1990, Paleolatitude distribution of Phanerozoic marine ooids and cements: Palaeogeography, Palaeoclimatology, Palaeoecology, v. 78, no. 1–2, p. 135–148, https://doi.org/10.1016 //0031-0182(90)90208-O.
- Oyhantçabal, P., Siegesmund, S., Wemmer, K., Presnyakov, S., and Layer, P., 2009, Geochronological constraints on the evolution of the southern Dom Feliciano Belt (Uruguay): Journal of the Geological Society, v. 166,

- p. 1075–1084, https://doi.org/10.1144/0016-7649 2008-122.
- Partin, C.A., and Sadler, P.M., 2016, Slow net sediment accumulation sets snowball Earth apart from all younger glacial episodes: Geology, v. 44, p. 1019–1022, https://doi.org/10.1130/G38350.1.
- Passchier, C.W., Trouw, R.A.J., Ribeiro, A., and Paciullo, F.V.P., 2002, Tectonic evolution of the southern Kaoko Belt, Namibia: Journal of African Earth Sciences, v. 35, p. 61–75, https://doi.org/10.1016/S0899-5362 (02)00030-1.
- Peltier, W.R., Tarasov, L., Vettoretti, G., and Solheim, L.P., 2004, Climate dynamics in deep time: Modeling the "snowball bifurcation" and assessing the plausibility of its occurrence, in Jenkins, G.S., McMenamin, M.A.S., McKey, C.P., and Sohl, L., eds., The Extreme Proterozoic: Geology, Geochemistry, and Climate: American Geophysical Union Geophysical Monograph 146, p. 107–124, https://doi.org/10.1029/146GM10.
- Porada, H., 1983, Geodynamic model for the geosynclinal development of the Damara Orogen, Namibia, South West Africa, in Martin, H., and Eder, F.W., eds., Intracontinental Fold Belts: Berlin, Springer, p. 502-538.
- Pullaiah, G., Irving, E., Buchan, K., and Dunlop, D., 1975, Magnetization changes caused by burial and uplift: Earth and Planetary Science Letters, v. 28, p. 133–143, https://doi.org/10.1016/0012-821X(75)90221-6.
- Raftery, A.E., 1995, Bayesian model selection in social research: Sociological Methodology, v. 25, p. 111–163, https://doi.org/10.2307/271063.
- Rapalini, A.E., 2006, New late Proterozoic paleomagnetic pole for the Rio de la Plata craton: Implications for Gondwana: Precambrian Research, v. 147, p. 223–233, https://doi.org/10.1016/j.precamres.2006.01.016.
- Rapalini, A.E., 2018, The assembly of Western Gondwana: Reconstruction based on paleomagnetic data, in Siegesmund, S., Basei, M.A.S., Oyhantçabal, P., and Oriolo, S., eds., Geology of Southwest Gondwana: Cham, Switzerland, Springer, Regional Geology Reviews, p. 3–18, https://doi.org/10.1007/978-3-319-68920-3\_1.
- Rapalini, A.E., Trindade, R.I.F., and Poiré, D.G., 2013, The La Tinta pole revisited: Paleomagnetism of the Neoproterozoic Sierras Bayas Group (Argentina) and its implications for Gondwana and Rodinia: Precambrian Research, v. 224, p. 51–70, https://doi.org/10.1016/j.precamres.2012.09.007.
- Rapalini, A.E., Tohver, E., Bettucci, L.S., Lossada, A.C., Barcelona, H., and Pérez, C., 2015, The late Neoproterozoic Sierra de las Ánimas Magmatic Complex and Playa Hermosa Formation, southern Uruguay, revisited: Paleogeographic implications of new paleomagnetic and precise geochronologic data: Precambrian Research, v. 259, p. 143–155, https://doi.org/10.1016 /j.precamres.2014.11.021.
- Raub, T.D., and Evans, D.A.D., 2005, Magnetostratigraphy of the type-Marinoan succession and correlatives throughout Australia: Geological Society of America Abstracts with Programs, v. 37, no. 7, p. 43.
- Reeves, C.V., de Wit, M.J., and Sahu, B.K., 2004, Tight reassembly of Gondwana exposes Phanerozoic shears in Africa as global tectonic players: Gondwana Research, v. 7, p. 7–19, https://doi.org/10.1016 /S1342-937X(05)70302-6.
- Robert, B., Besse, J., Blein, O., Greff-Lefftz, M., Baudin, T., Lopes, F., Meslouh, S., and Belbadaoui, M., 2017, Constraints on the Ediacaran inertial interchange true polar wander hypothesis: A new paleomagnetic study in Morocco (West African craton): Precambrian Research, v. 295, p. 90–116, https://doi.org/10.1016/j.precamres 2017.04.010.
- Rodríguez Piceda, C., Franceschinis, P.R., Escayola, M.P., and Rapalini, A.E., 2018, Paleomagnetismo del Grupo Santa Victoria en la sierra de Mojotoro, Salta: Aportes a la reconstruccíon paleogeogr'afica de Pampia en el Paleozoico Temprano: Revista de la Asociación Geológica Argentina, v. 4, p. 518–532.
- Sánchez-Bettucci, L., and Rapalini, A.E., 2002, Paleomagnetism of the Sierra de Las Animas Complex, southern Uruguay: Its implications in the assembly of western Gondwana: Precambrian Research, v. 118, p. 243–265, https://doi.org/10.1016/S0301-9268(02)00114-6.

- Schmidt, P.W., and Williams, G.E., 1995, The Neoproterozoic climatic paradox: Equatorial palaeolatitude for Marinoan glaciation near sea level in South Australia: Earth and Planetary Science Letters, v. 134, p. 107–124, https://doi.org/10.1016/0012-821X(95)00106-M.
- Schmidt, P.W., Williams, G.E., and McWilliams, M.O., 2009, Palaeomagnetism and magnetic anisotropy of late Neoproterozoic strata, South Australia: Implications for the palaeolatitude of late Cryogenian glaciation, cap carbonate and the Ediacaran System: Precambrian Research, v. 174, p. 35–52, https://doi.org/10.1016/j .precamres.2009.06.002.
- Sellers, W.D., 1969, A global climatic model based on the energy balance of the Earth-atmosphere system: Journal of Applied Meteorology and Climatology, v. 8, p. 392–400, https://doi.org/10.1175 //1520-0450(1969)008<0392:AGCMBO>2.0.CO;2.
- Sohl, L.E., Christie-Blick, N., and Kent, D.V., 1999, Paleomagnetic polarity reversals in Marinoan (ca. 600 Ma) glacial deposits of Australia: Implications for the duration of low-latitude glaciation in Neoproterozoic time: Geological Society of America Bulletin, v. 111, p. 1120-1139, https://doi.org/10.1130/0016-7606(1999)111<1120:PPRIMC>2.3.CO;2.
- Tauxe, L., and Watson, G.S., 1994, The fold test: An eigen analysis approach: Earth and Planetary Science Letters, v. 122, p. 331–341, https://doi.org/10.1016/0012-821X(94)90006-X.
- Tauxe, L., Kylstra, N.J., and Constable, C., 1991, Bootstrap statistics for paleomagnetic data: Journal of Geophysical Research: Solid Earth, v. 96, p. 11,723–11,740, https://doi.org/10.1029/91JB00572.
- Tauxe, L., Shaar, R., Jonestrask, L., Swanson-Hysell, N.L., Minnett, R., Koppers, A.A.P., Constable, C.G., Jarboe, N., Gaastra, K., and Fairchild, L., 2016, PmagPy: Software package for paleomagnetic data analysis and a bridge to the Magnetics Information Consortium (MagIC) Database: Geochemistry, Geophysics, Geosystems, v. 17, p. 2450–2463, https://doi.org/10.1002/2016GC006307.
- Temporim, F.A., Bellon, U.D., Domeier, M., Trindade, R.I.F., D'Agrella-Filho, M.S., and Tohver, E., 2021, Constraining the Cambrian drift of Gondwana with new paleomagnetic data from post-collisional plutons of the Araçuaí orogen, SE Brazil: Precambrian Research, v. 359, https://doi.org/10.1016/j.precamres .2021.106212.
- Tohver, E., D'Agrella-Filho, M.S., and Trindade, R.I.F., 2006, Paleomagnetic record of Africa and South America for the 1200–500 Ma interval, and evaluation of Rodinia and Gondwana assemblies: Precambrian Research, v. 147, p. 193–222, https://doi.org/10.1016/j.precamres.2006.01.015.
- Tohver, E., Weil, A.B., Solum, J.G., and Hall, C.M., 2008, Direct dating of carbonate remagnetization by <sup>40</sup>Ar/<sup>39</sup>Ar analysis of the smectite–illite transformation: Earth and Planetary Science Letters, v. 274, p. 524–530, https://doi.org/10.1016/j.epsl.2008.08.002.
- Torsvik, T.H., et al., 2012, Phanerozoic polar wander, palaeogeography and dynamics: Earth-Science Reviews, v. 114, no. 3–4, p. 325–368, https://doi.org/10.1016/j.earscirev.2012.06.007.
- Trindade, R.I.F., and Macouin, M., 2007, Palaeolatitude of glacial deposits and palaeogeography of Neoproterozoic ice ages: Comptes Rendus Geoscience, v. 339, p. 200–211, https://doi.org/10.1016/j.crte.2007.02.006.
- Trindade, R.I.F., Font, E., D'Agrella-Filho, M.S., Nogueira, A.C.R., and Riccomini, C., 2003, Low-latitude and multiple geomagnetic reversals in the Neoproterozoic Puga cap carbonate of Amazonia: Terra Nova, v. 15, p. 441–446, https://doi.org/10.1046/j.1365-3121.2003 00510 x
- Trindade, R.I.F., D'Agrella-Filho, M.S., Babinski, M., Font, E., and Neves, B.B., 2004, Paleomagnetism and geochronology of the Bebedouro cap carbonate: Evidence for continental-scale Cambrian remagnetization in the São Francisco craton, Brazil: Precambrian Research, v. 128, p. 83–103, https://doi.org/10.1016/j.precamres .2003.08.010.
- Trindade, R.I.F., D'Agrella-Filho, M.S., Epof, I., and Brito Neves, B.B., 2006, Paleomagnetism of Early Cambrian Itabaina mafic dikes (NE Brazil) and the final assem-

- bly of Gondwana: Earth and Planetary Science Letters, v. 244, p. 361–377, https://doi.org/10.1016/j.epsl.2005.12.039.
- Trindade, R.I.F., D'Agrella-Filho, M.S., Antonio, P.Y.J., and Teixeira, W., 2021, The Precambrian drift history and paleogeography of Congo–São Francisco craton, in Pesonen, L.J., Salminen, J., Elming, S-Å., Evans, D.A.D., and Veikkolainen, T., eds., Ancient Supercontinents and the Paleogeography of Earth: Amsterdam, Elsevier, https://doi.org/10.1016/B978-0-12-818533-9.00016-3.
- Van der Voo, R., 1990, The reliability of paleomagnetic data: Tectonophysics, v. 184, p. 1–9, https://doi.org/10.1016 //0040-1951/90/90116-P.
- Vincent, C., Fischer, A., Mayer, C., Bauder, A., Galos, S.P., Funk, M., Thibert, E., Six, D., Braun, L., and Huss, M., 2017, Common climatic signal from glaciers in the European Alps over the last 50 years: Geophysical Research Letters, v. 44, p. 1376–1383, https://doi.org/10 .1002/2016GL072094.
- Wallace, J.M., and Hobbs, P.V., 1977, Atmospheric Science: An Introductory Survey: New York, Academic Press.

- Weaver, C.E., 1958, The effects and geologic significance of potassium "fixation" by expandable clay minerals derived from muscovite, biotite, chlorite, and volcanic material: The American Mineralogist, v. 43, p. 839–861.
- Wu, J., Liu, Y., and Zhao, Z., 2021, How should snowball Earth deglaciation start: Journal of Geophysical Research: Atmospheres, v. 126, https://doi.org/10.1029 /2020JD033833.
- Yang, J., Jansen, M.F., Macdonald, F.A., and Abbot, D.S., 2017, Persistence of a surface freshwater ocean after a Snowball Earth: Geology, v. 45, p. 615–618, https://doi. org/10.1130/G38920.1.
- Zhang, Q.R., and Piper, J.D.A., 1997, Palaeomagnetic study of Neoproterozoic glacial rocks of the Yangzi Block: Palaeolatitude and configuration of South China in the late Proterozoic Supercontinent: Precambrian Research, v. 85, no. 3–4, p. 173–199, https://doi.org/10.1016/S0301-9268(97)00031-4.
- Zhang, S., Evans, D.A.D., Li, H., Wu, H., Jiang, G., Dong, J., Zhao, Q., Raub, T.D., and Yang, T., 2013, Paleomagnetism of the late Cryogenian Nantuo Formation and pa-

- leogeographic implications for the South China Block: Journal of Asian Earth Sciences, v. 72, p. 164–177, https://doi.org/10.1016/j.jseaes.2012.11.022.
- Zhang, S., Li, H., Jiang, G., Evans, D.A.D., Dong, J., Huaichun, W., Yang, T., Liu, P., and Xiao, Q., 2015, New paleomagnetic results from the Ediacaran Doushantuo Formation in South China and their paleogeographic implications: Precambrian Research, v. 259, p. 130– 142, https://doi.org/10.1016/j.precamres.2014.09.018.
- Zijderveld, J.D.A., 1967, Demagnetization of rocks: Analysis of results, in Collinson, D.W., Creer, K.M., and Runcorn, S.K., eds., Methods in Paleomagnetism: Amsterdam, Elsevier, https://doi.org/10.1016 /B978-1-4832-2894-5.50049-5.

SCIENCE EDITOR: MIHAI DUCEA ASSOCIATE EDITOR: MASSIMO MATTEI

Manuscript Received 12 October 2023 Revised Manuscript Received 13 March 2024 Manuscript Accepted 2 April 2024